THESIS

DISTRIBUTED SEASONAL AND ANNUAL MASS BALANCE MEASUREMENTS OF WOLVERINE GLACIER, ALASKA, USING GEODETIC SURVEYS AND EMERGENCE VELOCITIES

Submitted by

Lucas R. Zeller

Department of Geosciences

In partial fulfillment of requirements

For the Degree of Master of Science

Colorado State University

Fort Collins, Colorado

Summer 2021

Master's Committee:

Advisor: Daniel McGrath

Richard C. Aster
Stephen J. Leisz

ABSTRACT

DISTRIBUTED SEASONAL AND ANNUAL MASS BALANCE MEASUREMENTS OF WOLVERINE GLACIER, ALASKA, USING GEODETIC SURVEYS AND EMERGENCE VELOCITIES

Glaciers are key components of human-environmental systems worldwide. They are a source of fresh water for human consumption, crop irrigation, and hydroelectric power even during times of drought. Glaciers promote environmental and ecological heterogeneity by modulating stream temperatures and providing key nutrient, geochemical, and sediment fluxes, are popular tourism destinations, and introduce risks from natural hazards such as glacier-lake outburst floods. Glaciers have undergone dramatic retreat and thinning over the past 50 years, and these trends are predicted to accelerate through the 21st century.

Short term (seasonal to annual) measurements of glacier mass balance provide valuable insight on how glaciers respond to climatological forcings and the processes that drive those changes. However, in-situ measurements are prohibitively time consuming, logistically difficult, and prone to uncertainty, rendering them insufficient for global-scale analyses. The increasing availability of high-resolution geodetic products offers promising opportunities for measuring mass balance from a remote platform if the confounding effects of ice emergence velocities and firn compaction on surface elevation can be correctly constrained.

In this study, I present spatially and temporally distributed measurements of emergence velocities on Wolverine Glacier, Alaska, derived from three methods: 1) repeat Global Navigation Satellite System (GNSS) measurements of mass balance stakes, 2) modelled from

annual mass balance measurements and glacier thinning rates, and 3) a novel approach of differencing geodetic surveys and snow depths derived from ground penetrating radar surveys. These emergence velocities, in conjunction with estimates of firn compaction, were used to measure distributed mass balances of Wolverine Glacier over three winter seasons, one summer season, and two annual time periods via geodetic surveys. The three approaches to measuring emergence velocity showed overall agreement but had important spatiotemporal differences. Comparison of geodetic mass balances with in-situ point and glacier-wide average mass balances had root mean square errors of 0.42 and 0.46 meters water equivalent. These results indicate that if emergence velocities and firn compaction are carefully considered, geodetic methods can provide accurate measurements of distributed mass balances over seasonal and annual time frames, yielding an improved understanding of glacier response and trend over these time scales. Such an understanding will facilitate improvements in model physics and parameterizations, thus improving projections for the magnitude and timing of future glacier losses and their effects on downstream communities and ecosystems.

ACKNOWLEDGEMENTS

I would like to thank my advisor, Dr. Dan McGrath, for his continuous advice and support throughout this project. Thank you to my committee members, Dr. Rick Aster and Dr. Stephen Leisz, for agreeing to review my work and providing invaluable feedback. Countless individuals have contributed their time and effort towards data collection and analysis on Wolverine Glacier throughout the decades through the U.S. Geological Survey Benchmark Glacier Project. In particular, I would like to thank Louis Sass, Dr. Shad O'Neel, Chris McNeil, and Emily Baker for their direct contributions. This work was funded by the U.S. Geological Survey, Cooperative Ecosystems Studies Unit Agreement G19AC00166. Any use of trade, firm, or product names is for descriptive purposes only and does not imply endorsement by the U.S. Government.

And lastly, to my family, friends, fellow students, and the Fort Collins community. Thank you for being my support system throughout the years, without which I would not have the privilege to pursue my dreams.

TABLE OF CONTENTS

LIST OF TABLES

LIST OF FIGURES

LIST OF EQUATIONS

1. INTRODUCTION

1.1 Scientific Merit

Glaciers are key components of human-environmental systems worldwide. Mountain glaciers (not including Greenland and Antarctica) cover more than 700,000 km^2 of the Earth's surface, with a total volume of 158,000 km^3 (Figure 1; RGI Consortium, 2017; Farinotti et al., 2019). They are a source of fresh water for human consumption, crop irrigation, and hydroelectric power even during times of drought (Pritchard, 2019; Immerzeel et al., 2020). Glaciers are popular tourism destinations (Welling et al., 2015), promote environmental and ecological heterogeneity via temperature, nutrient, and sediment fluxes (Lane et al., 2017; Cauvy-Fraunié and Dangles, 2019), and introduce risk from natural hazards such as glacier-lake outburst floods (Stoffel and Huggel, 2012).

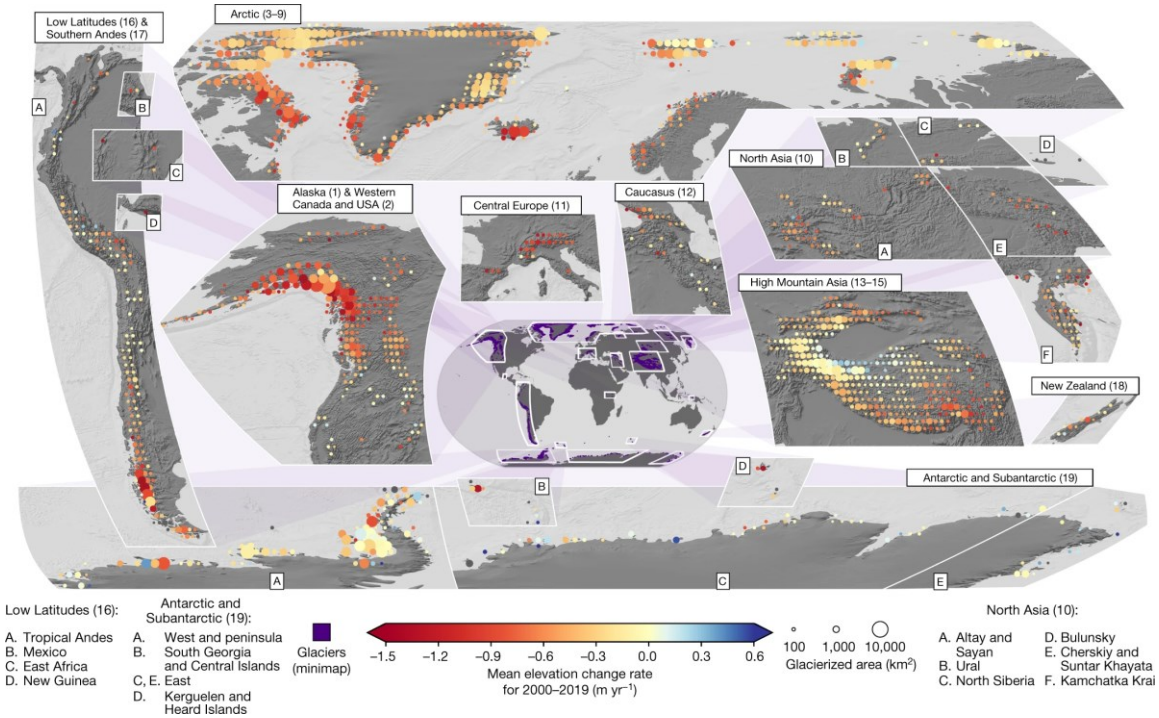

Figure 1: Global distribution of glaciers (center map, purple areas) and elevation change of glaciers over the 2000–2019 period (surrounding subplots) from Hugonnet et al. (2021).

Melting glaciers are one of the iconic images of climate change (Figure 2). Glaciers worldwide have been thinning and retreating since the mid-1900s in response to climate change, with mass loss accelerating over the past 20 years (Gardner et al., 2013; Zemp et al., 2019; Wouters et al., 2019; Ciracì et al., 2020; Hugonnet et al., 2021). Recent estimates suggest that anthropogenic forcing is responsible for essentially 100% of observed mass loss, with the possibility that glaciers may otherwise have actually gained mass without this forcing (Roe et al., 2021). These patterns of glacier melt, retreat, and thinning are predicted to continue and accelerate in the coming decades (Marzeion et al., 2012; Radić et al., 2013; Huss and Hock, 2015; Hock et al., 2019).

Mountain glaciers store a global sea level equivalent of 32 cm (Farinotti et al., 2019). The loss of this ice and the subsequent rise in sea level would cause the displacement of millions of people worldwide (Kulp and Strauss, 2019). Recent estimates of melt rates suggest that the mountain glacier contribution to global sea level rise since the mid-20th century is equivalent to that of the ice sheets despite containing only a small fraction of the ice sheet volume and area (WCRP Global Sea Level Budget Group, 2018; Zemp et al., 2019; Hugonnet et al., 2021).

Further effects will be felt on local (rather than global) scales as glacier changes impact downstream catchments (Huss et al., 2017). For example, changes in the timing and availability of meltwater will disrupt ecosystem characteristics such as water temperature, sediment supply, nutrient availability, and the normal seasonal patterns observed in each (Huss and Hock, 2018; Milner et al., 2017). Cryosphere related hazards are expected to increase as retreating glacier cause slope instability and glacial-lake outburst-floods become more frequent (Stoffel and Huggel, 2012). Predicting the localized impacts of glacial retreat is distinct from, and in ways

more difficult than, global-scale analyses due to the difficulties of collecting data at fine spatial and temporal scales over large regions.

Alaska contains approximately 27,000 glaciers covering an area of 87,000 km^2, constituting ~12% of the glacier area and volume worldwide (RGI Consortium, 2017). These glaciers are shrinking at a faster rate than any other region worldwide, accounting for 35% of the 21st century sea level rise that is due to melting glaciers (Zemp, 2019; Hugonnet et al., 2021). Concerning variations in stream hydrology, geomorphic hazards, and water quality as a direct result of these glacier changes have been observed and are predicted to continue (Moore et al., 2009).

The effects of glacier changes are already observable and will become more significant in the short term (in the coming decades) as mass loss accelerates and impacts accumulate. Mitigating and adapting to these changes is one of the most pressing challenges of the 21st century. Understanding the timing and magnitude of glacier mass loss will help society develop new mitigation approaches most effectively.

1.2 Glacier Mass Balance and Terminology

The purpose of this section is to introduce fundamental concepts of glaciers and glacier mass balance to an audience with no formal background in reading glaciological literature.

A glacier is defined as a large, perennial accumulation of ice and snow that originates on land and moves down slope under the influence of its own weight and gravity (https://www.usgs.gov/faqs/what-a-glacier). Glaciers form in regions where the accumulation of winter snow is not fully melted during the following summer. If this pattern is sustained over a long period of time, the snow will gradually compact under its own weight and

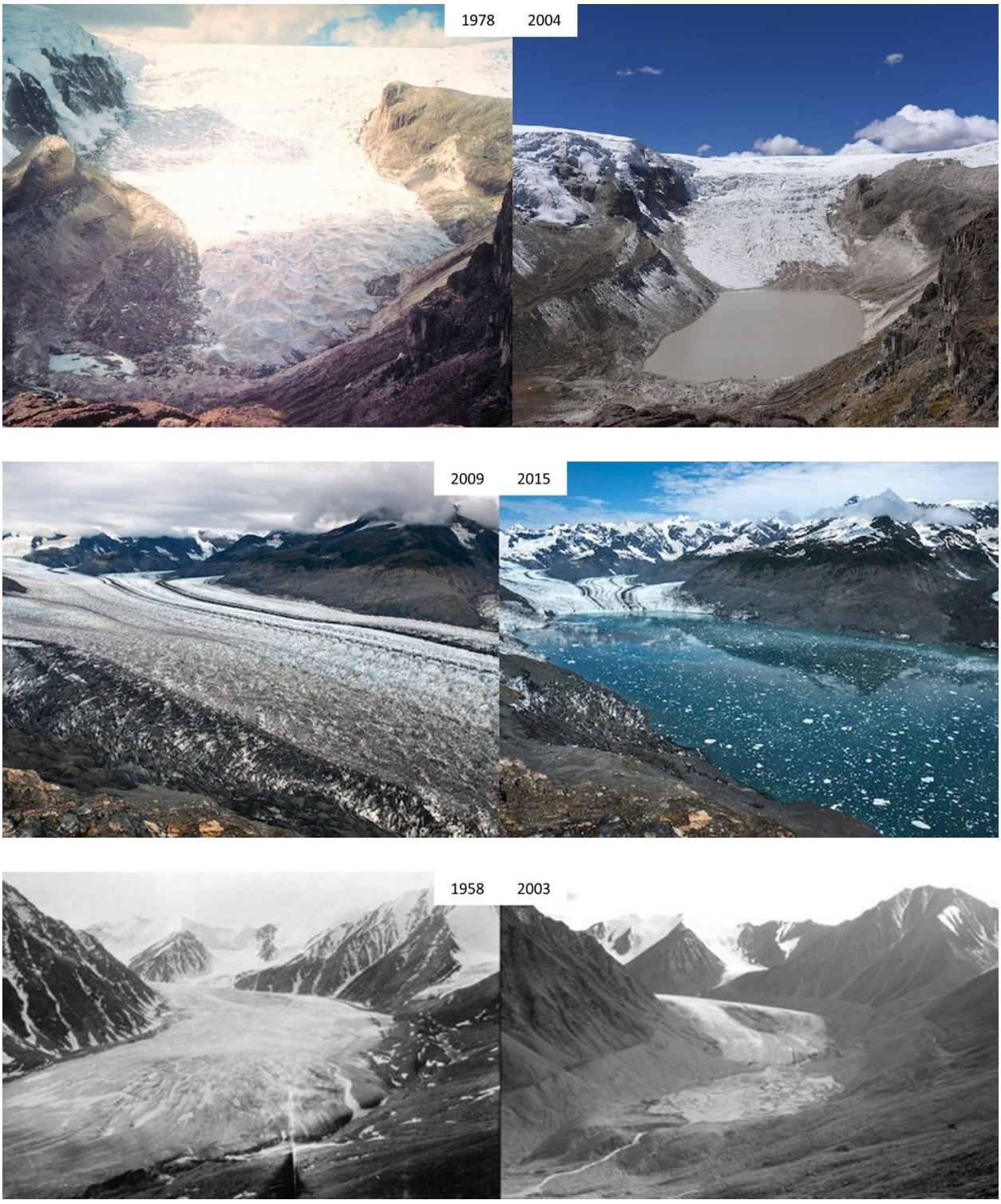

Figure 2: Photographs capturing the retreat of three glaciers over recent decades. Top images show Qori Kalis Glacier in Peru, middle shows Columbia Glacier in Alaska, and bottom shows McCall Glacier in Alaska. Photos courtesy of National Snow and Ice Data Center Glacier Photograph Collection and Extreme Ice Survey.

metamorphose into glacier ice. As the weight of glacier ice increases then the ice will begin flowing downhill by internal deformation and, in many cases, sliding at its base. As the glacier front flows downhill, it will move into areas where the annual temperature is warmer, causing less winter precipitation to fall as snow and more surface melt to occur in the summer. At some point there will be more melt occurring than snow accumulation, meaning the glacier will be losing mass in these areas. However, because the glacial flow will be transporting the accumulated mass from higher elevations down to these lower elevations, allowing the glacier to persist in these areas of mass loss. In a stable climate, the glacier will reach an equilibrium point where the mass gained at high elevations is equal to the mass lost at lower elevations, and the glacier flow transports ice between the two areas at such a speed that the glacier geometry remains constant. In this way, the glacier acts as a conveyor belt, transporting frozen water from high elevations down to lower, warmer elevations where it melts.

The amount of mass added to or removed from the glacier over a certain time span is referred to as the *mass balance*. The most commonly used units for glacier mass balance are *meters of water equivalent* (m w.e.), referring to the amount of water that would be produced if the ice/snow were melted into water. The density of glacier ice is approximately 900 kg/m^3, and snow densities range from 100 to 600 kg/m^3, meaning that one meter of glacier ice would be 0.9 m w.e. and one meter of snow can be anywhere from 0.1 to 0.6 m w.e. Snow that has persisted for more than one year but has not reached the density of ice is called *firn*, and has densities between those of snow and ice.

In this research, mass balance can be reported as a glacier-wide average or at a single point (the *point mass balance*). The part of a glacier at high elevations where annual mass gain (*accumulation*) is greater than mass loss (*ablation*) would have a positive annual mass balance,

whereas areas with annual mass loss would have a negative mass balance. These areas are called the *accumulation zone* and *ablation zone*, respectively. The elevation of the border between these two zones, where the annual mass balance is equal to zero, is called the *equilibrium line altitude* (ELA). The *annual mass balance* may be reported, identifying the mass change over the course of an entire year (from end-of-summer to end-of-summer), or the *seasonal mass balance*, identifying the mass change over just the summer or winter.

In our example of a glacier with a constant geometry in a stable climate, the winter mass balance could range from +1 m w.e. at the lowest elevations to +5 m w.e. at the highest elevations. The summer mass balance could then vary from –4 m w.e. to -2 m w.e. from lowest to highest elevations. The annual mass balance would be the sum of the winter and summer balance, so –3 m w.e. to +3 m w.e. The glacier-wide mass balance (assuming an even distribution of surface area over the elevation range) would then be zero.

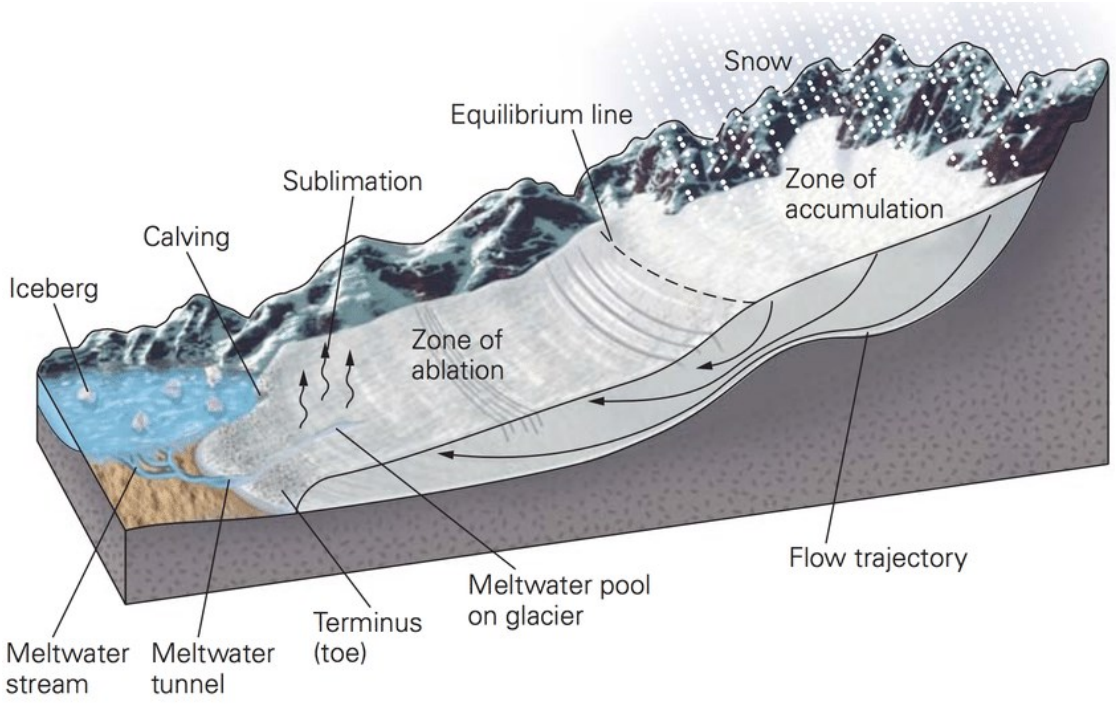

Figure 3: Diagram showing an idealized glacier geometry with important mass balance regimes and physical processes, from Marshak & Repcheck (2009)

In the real world, climate is constantly changing (globally and regionally), and glacier geometries are constantly responding to these changing forcings. Take, for example, the climate trends in Alaska where atmospheric temperature has been warming in the 21st century (Hersbach et al., 2020; Hugonnet et al., 2021). Warmer average temperatures lead to fewer days in which it is cold enough for precipitation to fall as snow and to warmer summer days. Less snow causes less mass to be gained by a glacier, and warmer summer days leads to more melt and more mass to be lost by the glacier. The result is a glacier-wide negative mass balance.

Under these conditions a glacier will be unstable and cannot exist in its current geometry. In order to reach a new equilibrium with the climate the glacier must change its geometry such that more of its surface area is in the accumulation zone and less in the ablation zone so that the glacier-wide mass balance approaches zero again. This is accomplished by the lowest elevation section of the glacier (the *terminus*) melting away, giving the appearance of the glacier retreating up to higher elevations. If the climate changes sufficiently such that the entire glacier surface is in the ablation zone, then the glacier will continue retreating until it eventually disappears.

The *response time* of a glacier refers to how quickly a glacier's geometry changes in response to climatic changes. Response times vary depending on many variables, such as the specific glacier size, location, thickness, area distribution, local climate, etc. However, the response time of glaciers are generally slower than the current rate of climate change, meaning that many glaciers are significantly out of equilibrium with the current climate. Even if the climate stabilized overnight, many glaciers would take decades to reach equilibrium.

It should be noted that there is significant variability in how glaciers are responding to climate worldwide. Not all regions have shown significant mass loss over the past 60 years (e.g. some parts of Central and South Asia), and not all glaciers within individual regions behave in

the same way. This results from regional variations in the ways that temperature and precipitation are changing (for regional differences in glacier responses). Local variations in variability in glacier mass balance is a results of more complex patterns such as topographic shading influences on heat fluxes, rain shadow effects, different glacier geometries leading to different amount of rain vs snow fall, etc. However, the vast majority of glaciers worldwide (including Wolverine Glacier) are losing mass and retreating.

1.3 In Situ Glacier Mass Balance Monitoring

Accurate measurements of glacier mass balance provide a valuable tool for assessing climatic impacts on glaciers and can help inform models of future glacier change (Marzeion et al., 2012; Radić et al., 2013; Clarke et al., 2015; Rounce et al., 2020).

Most approaches for measuring glacier mass balance from in-situ data involve the interpolation or extrapolation of point measurements. These point measurements are often made from mass balance stakes, which are long stakes (4 meters long) drilled into the glacier surface and revisited to track the change in the snow/ice surface, and thus the mass balance, throughout the year. Additional measurements of snow depth can be made by digging snow pits (which gives snow density as well as depth), snow probing, or using ground-penetrating radar. Field work is often timed to correspond to annual mass minima (end-of-summer) and maxima (end-of-winter) to allow separate calculation of winter, summer, and annual mass balances.

These point observations are then extrapolated across the entire glacier surface based on elevation (making *mass-balance profiles*), area-weighting (*site-index*), and parametrization based on terrain properties. In recent years the mass-balance profile fitting approach has become the standard approach, where linear or polynomial relationships are fit between the stake elevation

and mass balance observations. Glacier-wide balance is then calculated by applying this profile across the entire glacier surface. The assumption behind this approach is that elevation is the dominant control on mass balance, as colder temperatures at higher elevations result in less melt and more precipitation falling as snow. This approach works best with a large number of stakes distributed across the glacier, such that all mass balance regimes are well sampled. This is rarely the case, however, as mass balance is controlled by many variables (e.g. wind redistribution, topographic shading, snow avalanching) and the representativeness of a single location is difficult to quantify. This increases the uncertainty of glacier-wide mass balance measurements and possibly introduces bias into the results.

1.4 Geodetic Glacier Mass Balance Measurements

Direct in-situ observations of glacier mass balance are time consuming, logistically challenging, and prone to uncertainty, rendering them insufficient on their own for modern large-scale studies (O'Neel et al., 2019). Of the more than 200,000 glaciers worldwide, only a few hundred are actively monitored via in-situ observations (WGMS, 2020).

The increasing availability of remotely sensed geodetic products offers a promising approach for measuring glacier mass balance. Previous studies have utilized Structure-from-Motion (SfM) (Nolan et al., 2015), lidar (Helfricht et al., 2012; Deems et al., 2013), and satellite stereoscopic approaches (Shean et al., 2020) to create high-resolution digital elevation models (DEMs) of snow and ice surfaces. Repeat DEM surveys of a glacier surface can be used to measure the glacier's volume change over the intervening interval.

Over long time periods (>5 years), volume change can be interpreted as mass change by using a single density conversion to find a glacier-wide mass balance (Huss, 2013). However,

this approach does not give distributed mass balances, and applying geodetic approaches on short time scales (seasonal to annual) is difficult due to the confounding effects of surface mass balance, ice dynamics (referred to as ice emergence, emergence velocity, or flux divergence), and firn densification on the observed surface elevation change (Cuffey and Patterson, 2010; Sold et al., 2013).

Firn compaction is the process that occurs as snow layers gradually become denser until becoming ice. This process is driven by the weight of overlaying snow, meltwater percolation/refreezing changing the firn material structure, and the firn temperature. As the firn density increases, the surface lowers. However, this surface lowering and volume change does not equate to a change in mass, and interpreting this volume change as a mass change will result in a negative bias in geodetic mass balance measurements. Firn exists only in the accumulation zone of the glacier as it requires snow to persist for multiple years in order to form, and so firn compaction only needs to be considered in this region of the glacier.

Ice emergence is the vertical component of ice flow at the glacier's surface at a fixed point (Cogley et al., 2011). The magnitude of ice emergence is a product of the *flux divergence*, which refers to the difference between mass moving into and out of a vertical column, which is determined by the horizontal ice flow, glacier geometry, and glacier thickness. A positive flux divergence (more mass moving out of the column than into it) causes thinning of the glacier and thus a negative (downward) vertical ice flow. The opposite (negative flux divergence) causes thickening and thus positive vertical ice flow. Upward ice flow is referred to as *emergence* while downward ice flow is referred to as *submergence*. Generally, ice has a negative emergence velocity (*submergence*) in the accumulation zone and a positive emergence velocity (*emergence*) in the ablation zone. Greater magnitudes of emergence and submergence are found at the highest

and lowest elevations, and approach zero near the ELA. For the purposes of this research the terms *emergence*, *submergence*, *emergence velocity*, and *ice emergence* will be used interchangeably.

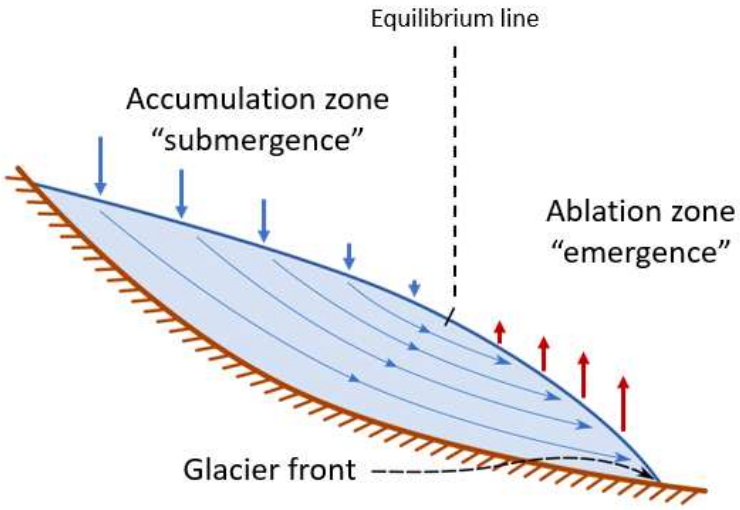

Figure 4: Cross section longitudinal view of a glacier which is flowing from left to right. Lines within the glacier indicate the flow path of ice, red and blue arrows above the glacier surface indicate direction and magnitude of ice submergence (blue) and emergence (red). Adapted from Spensberger (2013)

Accurately accounting for the effects of ice emergence and firn compaction is the primary limitation to fully realizing the potential of geodetic observations to derive seasonal to annual mass balances. Previous studies have addressed this via modeling approaches (Sold et al., 2013; Pope et al., 2016; Belart et al., 2017; Sass et al., 2017), using sparse in-situ point measurements of emergence velocities (Beedle et al., 2014; Réveillet et al., 2020), or have not explicitly accounted for these processes (Helfricht et al., 2014; Pelto et al., 2019). Accurate modelling and/or parametrization of these processes would facilitate the improved measurement of distributed seasonal and annual mass balances of mountain glaciers from remote sensing platforms on regional scales (i.e. over entire mountain ranges or watersheds). In order to achieve

this, comprehensive in-situ studies need to be conducted to capture the representative spatial and temporal variability of these processes.

1.5 Previous Work

An overview of recent studies that have attempted to account for emergence velocities and firn compaction in geodetic mass balance measurements is provided in the paragraphs below.

Sold et al. (2013) applied geodetic methods to measure winter mass balance (snow depths) of a single glacier (Fingelengletscher, Switzerland) in the Alps. They calculated distributed firn compaction and emergence velocities as a function of annual mass balance. Distributed mass balance was modelled for a five-year period based on meteorological data and tuned to in-situ measurements. They used the assumption that annual firn compaction was equal to a single annual accumulation layer transformed from end-of-year snow density to ice. Ice emergence was similarly modelled as the ratio between the mass balance (multiplied by –1) and ice density, corrected for annual geometry changes that may signal an imbalance between ice flow and mass balance. They then compared their geodetic measurements with in-situ snow depth measurements, finding that the two datasets showed good agreement.

Beedle et al. (2014) measured annual mass balances of a single glacier in British Columbia (Castle creek Glacier) over three years from 2009 – 2011. They measured emergence velocities at discrete points and then extrapolated these measurements across the entire glacier surface. In the accumulation zone they did not explicitly account for firn compaction, however their emergence measurements implicitly account for it without attempting to separate the effects

of the two processes. The year-to-year differences in emergence velocities seem significant but are not quantified in their paper.

Pope et al. (2016) calculated emergence velocities of the Langjökull ice cap in Iceland (~900 km^2) over multi-year periods through the use of repeat DEMs (spaced apart by multiple years) and a mass balance model. Due to modelling over long time periods in a relatively stable climate, they were able to discount the effects of firn compaction by assuming that net firn thickness remained constant. They were able to observe long-term similarities in emergence velocities, apart from distinct variations on surge-type glaciers.

Belart et al. (2017) applied high resolution (sub-meter) satellite imagery to estimate winter snow depths over the Drangajökull ice cap in Iceland (143 km^2). They estimated firn compaction in a similar manner to Sold et al. (2013) but used only a single year of distributed mass balance data under the assumption that it reliably represented the average annual mass balance. Two methods of calculating ice emergence were tested, the first modelled using annual mass balance in a manner similar to Sold et al. (2013), and the second by using a full-Stokes ice flow model. It should be kept in mind that the dynamics of an ice cap of the size and climatic region covered in Pope et al. (2016) and Belart et al. (2017) are substantially different from those of temperate mountain glaciers.

Pelto et al. (2019) calculated annual and winter mass balances for six glaciers in the Canadian Rockies over a time period of four years using repeat lidar surveys. They did not attempt to calculate distributed mass balances, instead measuring only glacier-wide averages by partitioning observed elevation change into varying densities based on the distribution of snow, firn, and ice across the glacier surface.

Réveillet et al. (2021) measured ice emergence over the course of one year in the accumulation zone of a glacier in the Alps (Mer de Glace) by extrapolating point measurements in a similar manner to Beedle et al. (2014). They did not explicitly account for firn compaction, although their setup for measuring emergence would have included the effects of at least a portion of this lowering. They were able to measure distributed mass balance and emergence velocities over sub-seasonal time scales, finding that the emergence velocities showed little seasonal variation.

1.6 Study Objectives

The goal of this study is to measure the distributed mass balance of Wolverine Glacier, Alaska over seasonal and annual time scales using repeat geodetic surveys. Multiple approaches for constraining ice emergence and firn compaction are considered, and geodetic mass balance measurements are compared to in-situ measurements to evaluate the accuracy of these approaches.

2. STUDY AREA

Wolverine Glacier is located in the Kenai Mountains of Alaska, approximately 100 km southeast of Anchorage and 50 km from the coast (Figure 5). The Kenai Peninsula has a mild coastal maritime climate that is characterized by relatively warm temperatures and abundant precipitation. In 2018, the glacier covered an area of 15.6 km^2 in a 24 km^2 basin, shrinking from an area of 17.1 km^2 in 1969, corresponding to a cumulative mass balance of –20 meters water equivalent (m w.e.) over this ~50-year interval (O'Neel et al., 2019). The majority of this mass loss occurred between 1990 and present day, and has accelerated in the 2000s, which is in line with regional mass loss rates and trends (e.g., Larsen et al., 2015; Zemp et al., 2019; Hugonnet et al., 2021). The glacier has a southerly aspect, with elevations ranging from ~500 m at its narrow terminus to over 1600 m in the upper reaches of the accumulation zone, with a long-term (20-year average) equilibrium line altitude (ELA) of 1226 m. Typical annual mass balances over the same period range from –7.0 to +4.3 m w.e./yr at the terminus and upper accumulation zone respectively.

Wolverine Glacier is part of the U.S. Geological Survey (USGS) Benchmark Glacier Project, which maintains long-term monitoring of mass balance, glacier geometry, climate, and streamflow on five glaciers in Alaska, Washington, and Montana. Wolverine Glacier has been monitored since 1966, making it one of the longest running records of glacier mass balance in North America. From 1966 to 2009 the mass balance was measured using three mass balance stakes: one in the ablation zone, one in the accumulation zone, and one in the vicinity of the ELA. Since 2009, additional stakes have been added to better capture the spatial variability in mass balance and the current array is comprised of eight stakes.

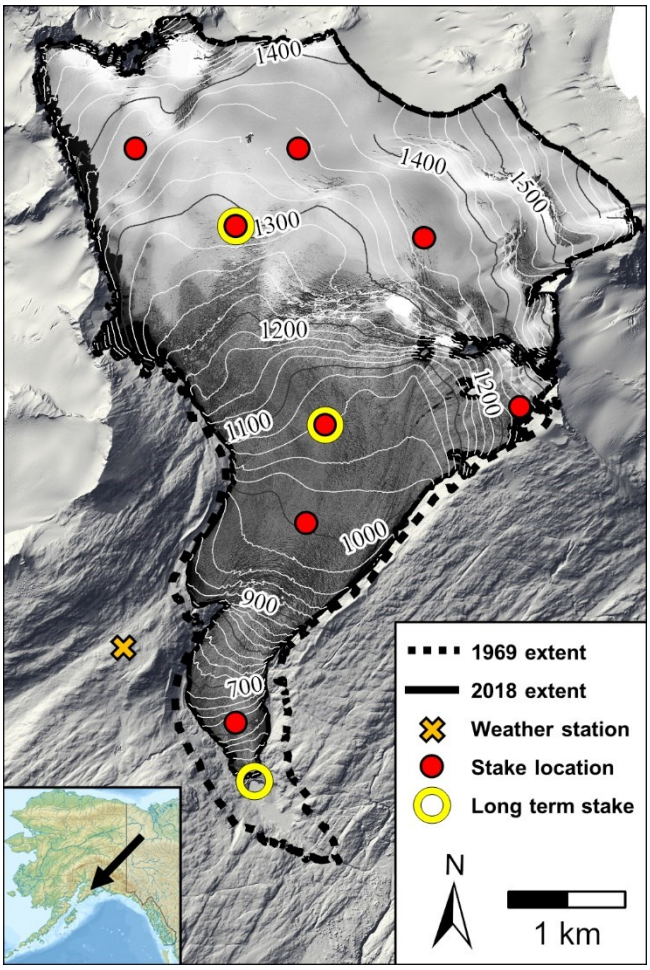

Figure 5: Wolverine Glacier study area, showing the glacier geometry and location of modern (red dots) and historical (yellow circles) mass-balance stakes and the meteorological station used in this study (yellow X). Elevation contours are given in meters. Dashed outline shows the glacier's extent in 1969. The glacier surface is shown as an orthoimage from the end-of-summer 2018, clipped to the modern extent. Off-glacier terrain is illustrated by a DEM-derived hillshade. Inset shows the glacier's location on the Kenai Peninsula in Alaska.

Two meteorological stations are operated proximal to Wolverine Glacier, one located at 990 m elevation near the western edge of the glacier and one located at 1420 m elevation ~1 km west of the glacier (USGS, 2020). The weather stations measure temperature, wind speed and direction, precipitation, relative humidity, and solar radiation. The long-term average annual air temperature at the Wolverine weather station (990 m elevation) is –1 °C, with daily average temperatures ranging from –25 °C to 15 °C (Baker et al., 2019). Average annual measured

precipitation at the weather station is 1100 mm, however this is likely not representative of the actual annual precipitation in the basin, as there is significant undercatch for snowfall which constitutes the majority of precipitation (Mayo et al., 1992). Only data from the 990 m elevation meteorological station is used in this study.

3. DATA AVAILABILITY

3.1 Digital Elevation Models

Seven digital elevation models (DEMs) of Wolverine Glacier were acquired between 2015 and 2020 (Table 2) for calculation of emergence velocities, winter mass balance, and annual mass balances (Table 1). When combined, these DEMs allow surface elevation change to be measured for time periods corresponding to three winter, one summer, and two annual balance periods. DEMs were collected using a variety of methods, with four collected via aerial lidar, two from aerial SfM, and one from satellite stereoscopic imagery.

Fall DEMs were co-registered to the fall 2019 DEM using a universal method (Nuth and Kaab, 2011) by selecting areas of stable, snow-free ground over which to minimize misalignment. Co-registration of spring DEMs is difficult due to the widespread snow cover removing the majority of suitable off-glacier stable control points (e.g., Pelto et al., 2019). Thus, for spring DEMs 3–4 coincident stable features (e.g., consistently exposed bedrock, man-made structures) were identified, and a constant x/y/z offset was applied to each DEM to manually align them with the fall 2019 DEM.

Five additional historic DEMs (Table 2; McNeil et al., 2019) between 1972 and 2012 were used for calculation of long-term thinning rates.

3.2 End-of-winter Snow Depths

Ground-penetrating radar (GPR) is an effective method of measuring snow depth in both glaciated and non-glaciated environments (e.g. Kohler et al., 1997; Machguth et al., 2006;

McGrath et al., 2015; Sold et al., 2015). End-of-winter snow depths on Wolverine Glacier were measured using GPR in the spring of three years (Table 2) as described in McGrath et al. (2018). Common-offset GPR surveys were conducted using a 500 MHz Sensors and Software pulseEkko Pro system from a snowmobile or helicopter platform. Survey tracks were similar each year, with an attempt to collect data spanning the full range of glacier terrain parameters (elevation, aspect, slope, etc…) while minimizing safety hazards (crevasses, avalanches).

Table 1: Timeframes over which mass balances were measured geodetically, with dates of corresponding DEM, GPR, and USGS mass balance measurements. All dates are listed in mm/dd/yyyy format. 2016 summer does not have DEM dates listed because it was calculated as the difference between the 2016 winter and 2016 annual balance.

Timeframe	DEM 1 date	DEM 2 date	USGS Mass Balance Dates	GPR Date
2016 Winter	08/13/2015	05/05/2016	09/09/2015 - 05/10/2016	04/21/2016
2017 Winter	09/10/2016	05/05/2017	10/15/2016 - 05/29/2017	04/26/2017
2020 Winter	09/20/2019	05/02/2020	09/17/2019 - 04/15/2020	05/13/2020
2016 Annual	08/13/2015	09/10/2016	09/09/2015 - 10/15/2016	---
2019 Annual	09/12/2018	09/20/2019	10/02/2018 - 09/17/2020	---
2016 Summer	---	---	05/10/2016 - 10/15/2016	---

Table 2: Acquisition platform of all 12 DEMs used. All dates are listed in mm/dd/yyyy format.

DEM Date	DEM platform
09/13/1972	aerial SfM
08/03/1979	aerial SfM
09/27/1995	aerial SfM
09/17/2008	satellite photogrammetry (classified)
08/22/2012	satellite photogrammetry (Worldview)
08/13/2015	aerial SfM
05/05/2016	aerial lidar
09/10/2016	aerial lidar
05/05/2017	aerial SfM
09/12/2018	satellite photogrammetry (Worldview)
09/20/2019	aerial lidar
05/02/2020	aerial lidar

Survey tracks in 2017 represent the "standard" lines that were collected. Helicopter surveys in 2016 were completed in a grid pattern covering most of the glacier area, and a subset of the data was selected within 150 m of the ground-based surveys to maintain consistency. GPR observations in 2020 were limited largely to the ablation zone and were supplemented with sparse point observations at higher elevations from mass balance stakes. Surveys were conducted during spring mass balance field campaigns, at a time close to the expected maximum snow water equivalent (SWE) on the glacier.

Radargrams were processed using ReflexW-2D by applying a time-zero correction, dewow filter, and other filters as needed. Manual picking of the annual layer boundary (bottom of the season snowpack) was guided by ground-truth point observations from probed snow depths in the ablation zone and shallow snow cores at mass balance stake locations in the accumulation zone.

Snow density (ρ) was measured in ~5 snowpits/cores across the glacier elevation range. Snow densities did not show a consistent elevation dependency, allowing for a single glacier-wide density to be used each year (McGrath et al., 2018). Radar velocity (v_s) was calculated from an empirical relationship based on the density (Kovacs et al., 1995) and direct comparison between observed in-situ snow depth and radar twt at probe and core locations mentioned previously. Snow depth and SWE were calculated using two-way travel time (twt), density, and velocity measurements using Eq. (1).

$$SWE = \left(\frac{twt}{2}\right) * v_s * \rho \tag{1}$$

Snow depth observations were extrapolated across the glacier surface at 10 m spatial resolution using statistical methods related to terrain parameters (McGrath et al., 2018). This approach uses the assumption that terrain parameters can be used as proxies for the physical

processes that distribute snow across the landscape. Terrain parameters were calculated from a fall 2015 DEM, and the same values used each year. The 2015 DEM was resampled to 10 m resolution before calculating terrain parameters. GPR snow depth observations in each year were similarly aggregated to 10 m resolution by taking the median of all observations within each pixel.

A regression tree model was then implemented to extrapolate GPR-derived snow depth observations across the entire glacier surface each spring. The terrain parameters used were: curvature, northness, eastness, and Sb: a parameter introduced by Winstral et al. (2002) related to wind sheltering effects from surrounding topography and thus potential for wind scouring and drifting. Prior to implementation, the SWE elevation gradient was removed from observations using a least-squares regression, as elevation was the dominant independent variable and observations did not cover the entire elevation range.

3.3 Mass Balance Stakes

The mass balance stake network has been the primary emphasis of the monitoring effort at Wolverine Glacier since the inception of the Benchmark Glacier Program in the 1960s. For the majority of the mass balance record only three sites were monitored, with stakes placed in areas representing the ablation zone, near the ELA, and the accumulation zone. Stakes are re-installed every 1–2 years on average in order to maintain continuity of the sampling locations across the record and to ensure ice flow did not carry them into new mass-balance regimes. In 2010 the network was expanded to seven stakes to better capture the spatial variability in mass balance.

Mass balance is measured seasonally at each stake to determine summer, winter, and annual point balances. Additional snow probing, snow pit, and snow coring measurements are

taken to measure snow density and small-scale spatial variability in mass balance at each site. These point measurements are used to determine glacier-wide mass balance and mass balance profiles (see Section 1.1.3). A reanalysis effort by O'Neel et al. (2019) incorporated geodetic datasets to provide a consistent aggregation of these point mass balance measurements and glacier-wide solutions.

3.4 Firn Cores

Three firn cores were collected from the accumulation zone at an elevation of ~1350 m at the end of summer in 2016, 2017, and 2019. Cores were drilled using a 56 mm diameter Felix snow corer. Samples were cut and weighed in sections ranging in length from ~0.1 to 0.5 m to measure density. Cores were drilled to a depth of ~20 to 25 m, where densities approach that of ice. Coring sites were consistent from year to year, and a mass balance stake was installed nearby (within 30 m), providing winter, summer, and annual surface mass balance measurements from 2016 to present.

3.5 Meteorological Data

The two weather stations at Wolverine Glacier provide meteorological data at 15 minute, 60 minute, and daily intervals. Short gaps (up to 3 days) in the datasets were filled using linear interpolation, and longer gaps were filled via monthly regression from a weather station in Seward, AK (40 km away; O'Neel et al., 2019). Data from the lower elevation station was incorporated into mass balance analyses to align observations with the precise timing of mass balance maxima and minima on the glacier surface. Daily values for air temperature and

precipitation from the lower weather station (990 m elevation) were used in this study (see Section 4.4 PDD model) (Baker et al., 2019).

4. METHODS

4.1 Geodetic Mass Balance Calculations

Distributed surface mass balances are measured geodetically by using Eq. (2) to partition geodetically observed elevation changes into three processes that affect glacier surface height (Δz): surface mass balance (b_{sfc}), firn compaction (f), and ice emergence (w_s) (Cuffey and Patterson, 2010).

$$\Delta z = b_{sfc} + f + w_s \tag{2}$$

Each term on the right represents the vertical change in surface height at a single point, measured in length scale, with positive values representing an upward shift (rising surface) and negative values a downward shift. Surface mass balance can be either positive (snow accumulation) or negative (snow/ice melt). Firn compaction always results in a lowering of the surface, and so it is exclusively a negative value. Ice emergence can be either positive or negative, with positive values (emergence) expected in the ablation zone and negative values (submergence) in the accumulation zone.

DEM differencing gives Δz, and the combined effects of firn compaction and ice emergence ($w_s + f$) is the expected elevation change given no changes in mass balance. The difference between the observed and expected surface elevation changes is the change in surface elevation due to changes in surface mass balance, as shown in Eq. (3).

$$b_{sfc} = \Delta z - (w_s + f) \tag{3}$$

The value of b_{sfc} represents a change in volume due to accumulation and ablation. This volume is converted to a change in mass by using varying densities for snow, firn, and ice according to the following rules:

1) areas with positive b_{sfc} are assumed to be snow accumulation, and a density of 440 kg/m^3 is used for end-of-winter observations and 600 kg/m^3 for end of summer observations (based on typical in-situ observations from Wolverine Glacier)
2) areas with negative b_{sfc} are given a firn density of 750 kg/m^3 if the area contains firn (as determined by the firn model) or an ice density of 900 kg/m^3 if firn is not present.

Two different emergence velocity products are used for mass balance measurements: the GPR emergence product, and the modelled emergence product (see section 4.2 Emergence Velocity Calculations for a description of each). Emergence velocities are assumed to be constant throughout the year, allowing the velocity field to be scaled to the precise length of time between DEM surveys. Seasonality in firn compaction rates are treated in a similar manner, with annual firn compaction scaled to the time between DEMs.

Geodetic mass balances are calculated for six time periods, encompassing three winter seasons and two annual balance years (Table 1). An additional summer mass balance is calculated in 2016 via differencing between the annual and winter balance. The calculations are repeated for each of the two emergence velocity products. These measurements were compared to in-situ mass balance observations from the distributed stake network, GPR surveys, and glacier-wide average mass balances to evaluate the performance of the geodetic approach. The

mass balance model (Section 4.4) is used to account for mass balance changes between the DEM survey dates and the in-situ observations.

4.2 Emergence Velocity Calculations

Three methods for calculating ice emergence velocities are presented: 1) through the differencing of seasonal DEMs and accounting for snow accumulation and firn compaction (referred to as the GPR emergence method due to the GPR-derived snow depths); 2) repeat GNSS measurement of mass balance stakes (referred to as the stake emergence method); and 3) modelling the emergence velocity based on annual mass balance records (referred to as the modelled emergence method). Each of the three approaches is described below.

4.2.1 GPR Emergence

The GPR approach for measuring ice emergence isolates the effect of ice emergence on glacier surface elevation change. By rearranging from Eq. (2) to Eq. (4), emergence velocities w_{s_GPR} can be calculated by individually solving for Δz, b_{sfc}, and f.

$$w_{s\_GPR} = \Delta z - b_{sfc} - f \tag{4}$$

Δh is measured over a winter season using repeat DEM measurements of the glacier surface and differencing the products. The first DEM is collected in the late fall near the annual mass balance minima of the glacier, and the second DEM is collected the following spring near the annual mass balance maxima. The surface elevation of the fall DEM is subtracted from the surface elevation of the spring DEM, giving a distributed measurement of surface elevation changes between the two surveys.

Because elevation change is measured over the winter season, minimal surface melt occurs and the majority of surface mass balance change, b_{sfc}, is snow accumulation. Distributed end-of-winter snow depths were measured using GPR surveys timed to coincide closely with DEM collection. A mass balance model was used to account for any mass balance changes occurring between the DEM and GPR surveys, and any ice melt occurring over the winter was estimated from mass balance stakes (O'Neel et al., 2019). GPR surveys give distributed snow depth estimates across the entire glacier surface, while the mass balance model and ice melt estimates are elevation-dependent profiles.

Firn compaction in the accumulation zone, f, was accounted for using the Herron and Langway (1980) model (see Section 4.3). Annual mass balances and snow densities were inputs for the model, resulting in estimated magnitudes of surface lowering due to firn compaction in annual increments. In the absence of additional constraints, we assumed that the rate of compaction was constant with time and thus the annual values were scaled to the length of time between DEM surveys.

All inputs in the emergence calculations (DEMs, snow depth, firn compaction) were resampled to 10 m resolution and aligned to a common grid. GPR emergence is calculated over three winter seasons: 2016, 2017, and 2020. Values from each year were scaled to annual velocities using the number of days between DEM surveys. Each emergence velocity product was smoothed using a low-pass median filter with a 5x5 kernel size to remove physically impossible values (from artifacts of the methodology, such as advecting topography/crevasses and inaccurate snow depths). Due to the difficulties of co-registering the spring DEMs, a constant vertical offset (ranging from 0.1 to 1.17 m) is applied to each spring DEM such that the glacier-wide sum of emergence velocities is equal to zero to follow mass continuity. These

vertical offsets in spring DEMs are carried forward to subsequent geodetic mass balance measurements.

4.2.2 Stake Emergence

Point measurements of ice emergence are obtained by using repeat GNSS measurements of mass balance stakes. Emergence velocities are calculated in a Lagrangian frame of reference (as opposed to the Eulerian frame of reference in the GPR emergence method) by measuring a stake location at two points in time and using Eq. (5), where Δz_0 is the observed change in elevation of the bottom of the stake, Δz_e is the expected change in the elevation of the stake, and t is the time between GNSS measurements. Δz_e is calculated by differencing the elevation of the glacier surface at the stake's start and end position from a single DEM.

$$w_{s\_stake} = \frac{\Delta z_0 + \Delta z_e}{t} \tag{5}$$

There were 125 stake GNSS measurements made between 2015 and 2019, from which 90 repeat measurement pairs were used to calculate emergence velocities. The maximum time between GNSS measurements was 1 year, and pairs separated by a longer period were discarded. In cases where a stake was measured three times in a single year (i.e. fall 2015, spring 2016, and fall 2016) then all three combinations of stake pairs were used to calculate velocity (fall 2015 to spring 2016, spring 2016 to fall 2016, and fall 2015 to fall 2016). A single DEM from spring 2016 was used to calculate Δz_e for all stake pairs.

Earlier stake velocity measurements from 1975 to 1995 were also analyzed (Mayo et al., 2004). Three locations spanning the elevation range of the glacier were surveyed multiple times per year over the twenty-year time period, giving 226 repeat pairs. Stake locations and glacier surface heights were measured relative to geodetic monuments within a local frame of reference

using theodolites. Emergence velocities were measured in a Eulerian frame of reference, calculated as the difference between glacier surface elevation change at the same point in space and the change in surface height due to mass balance processes (as measured by mass balance stakes in the immediate vicinity). This approach is similar to the GPR emergence method presented previously but using in situ observations rather than remotely sensed measurements (DEMs and GPR).

4.2.3 Modelled Emergence

The third approach for calculating ice emergence is by modelling it based on the average annual surface mass balance as described in Sold et al. (2013). With the assumption that the glacier is in equilibrium and has a constant geometry, the emergence velocity is counteracting the effect of a single layer of ice being added or removed each year in order to keep the surface at the same elevation. Thus, the emergence velocity is equal to the average annual mass balance, b_a (m w.e.), divided by the density of glacier ice, ρ_{ice} = 900 kg/m^3, multiplied by –1. Sold et al. (2013) introduced an additional term, Δz_{thin}, for a glacier in disequilibrium to account for an imbalance between ice flow and mass balance. This term is equal to the long-term annual thinning rate of the glacier (thinning gives a negative Δz_{thin} and thickening a positive value, units are m/yr) (Eq. (6)).

$$w_{s\_mod} = \Delta z_{thin} - b_a/\rho_{ice} \tag{6}$$

This method is applied to calculate elevation profiles of emergence velocities on Wolverine Glacier using stake-derived annual mass balance profiles (O'Neel et al., 2019). Emergence values are calculated for both recent years (2015–2019) and three other historical

time periods. Δz_{thin} is calculated for each period by differencing DEMs at the start and end of the period and applying a piecewise linear fit to determine elevation profiles of surface lowering (Figure 6).

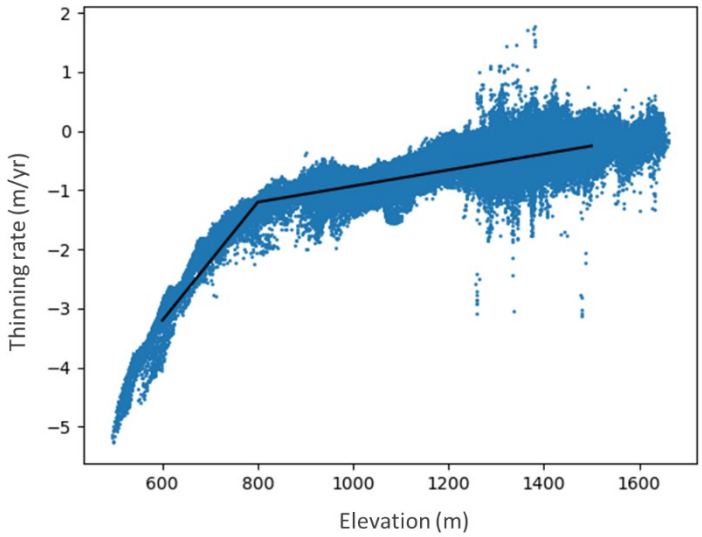

Figure 6: Example plot of the long-term thinning rate of WG from 1995 to 2015, used in the calculation of the modelled emergence velocities. Each point represents the annual lowering rate of a 10x10 meter pixel over the time frame, plotted by elevation (x-axis). Black line indicates the piece-wise linear fit used in the emergence modelling calculation.

4.3 Firn Compaction Model

Surface lowering due to firn compaction was modelled using the Herron and Langway model (1980; HL model) as implemented by Reeh (2008) and Huss (2013). Using Eqs. (7)-(9), it calculates the density of a firn layer (ρ_{firn}) after a certain number of years (t) based on the mean annual firn temperature in Kelvin (T), initial firn density ($\rho_{firn,0}$), and mean annual mass balance (b) (i.e. the weight of overlaying snow added each year). The density of ice (ρ_{ice}) is set to 900 kg/m^3 and the density of water (ρ_{water}) is 1000 kg/m^3. R is the gas constant, 8.31446 J/(°K·mol), and f is a tuning factor that was empirically determined by Herron and Langway (1980) as 575. $RF(t)$ accounts for increasing densification due to refreezing of percolating meltwater.

$$\rho_{firn}(t_0, t) = \rho_{ice} - \left(\rho_{ice} - \rho_{firn,0}\right) * \exp(-c * t) + RF(t) \quad (7)$$

$$c = k_1 \sqrt{b * \frac{\rho_{ice}}{\rho_{water}}} \quad (8)$$

$$k_1 = f * \exp\left(\frac{-21400}{R * T}\right) \quad (9)$$

The HL model was developed for steady state conditions, meaning that the annual balance, temperature, and initial density are assumed constant from year to year. Reeh (2008) showed that the model is suitable for non-steady state conditions and introduced the $RF(t)$ factor to account for the effects of refreezing of meltwater. $RF(t)$ is approximated here by assuming an end-of-winter temperature profile which linearly increases form –5 °C at the surface to 0 °C at 5 meters depth and allowing for complete latent heat exchange to refreeze percolating meltwater (Huss, 2013).

The firn column is modelled in one-year time steps, with a new firn layer introduced each year at the end-of-summer. The initial density of each layer ($\rho_{firn,0}$) is assigned based on in-situ snow pit measurements collected at the end-of-summer each year from 2000 to 2019 (ranging from 550 to 640 kg/m^3). For prior years, the 2000–2019 mean value of 600 kg/m^3 was used. Average annual mass balance for each time step was calculated as the mean balance of the layers which have been deposited on top of it. The model accounts for negative balance years by removing mass from the top of the firn column (melting) while still allowing for compaction in the remaining firn. A minimum increase in layer density is assigned to increase rates of densification at higher densities (Huss, 2013). Total surface lowering from firn compaction (from fall to fall) is then calculated as the sum of compaction of each individual layer in a given year.

Distributed annual mass balance products were estimated for use in the firn model in a two-step process using stake-derived mass balance profiles (from O'Neel et al., 2019). First, distributed end-of-winter mass balances were calculated by distributing the winter mass balance profiles to match the typical spatial distribution of end-of-winter snow depths observed in GPR surveys over the course of 5 years (2013–2017). For each year, the ratio between each 10x10 m pixel's balance and the mean balance of all pixels within 50 m elevation of it was computed. The pixel-wise mean of the five years was calculated to give a single map showing the balance variation of each pixel with respect to its elevation. The maximum average variation allowed was two (indicating winter balances twice as high as the winter balance profile would predict) to minimize the effect of a handful of outliers. Distributed winter balance maps were then calculated for each year by multiplying the expected balance of a pixel (given its elevation, from the winter balance profiles) by the average variation.

Summer balance profiles (elevation dependent, not fully spatially distributed) were added to the distributed winter balance products, giving an approximation of the distributed annual balance in each year. No attempt was made to spatially distribute summer balances within elevation bands given the lack of observations needed. Distributed balance maps were calculated each year for the 2000-2019 period. For prior years, annual balance profiles were used.

4.4 Mass Balance Model

A mass balance model (van Beusekom et al., 2010; O'Neel et al., 2019) was used to estimate mass balance changes over short time periods to temporally align observations occurring on different dates (e.g. stake observations and DEMs). The model uses daily average temperature and precipitation values to approximate accumulation and ablation at each point.

The net mass balance is considered to be the sum of accumulation and ablation. Ablation, a, is modelled using a positive degree-day approach (Eq. (10)), where $T_{(T>0)}$ is a positive air temperature estimate (determined using a lapse rate of –6.5 °C/km) and $k_{s,i}$ is a scaling factor for snow or ice determined empirically from historic mass balance and weather observations. Accumulation, c (Eq. (11)), is estimated by assuming that precipitation falls as snow at temperatures below 1.7 °C (U.S. Army, 1956) and scaled using γ to account for differences in measured precipitation at the weather station and historical observations across the glacier (O'Neel et al., 2019) Specific scale factors, $k_{s,i}$, were determined for each long-term mass balance stake and a glacier-wide average used for other locations.

$$a = T_{(T>0)} * k_{s,i} \tag{10}$$

$$c = T_{(T<1.7)} * \gamma \tag{11}$$

5. RESULTS

Results will be presented in the order in which they are used in the analyses. First, a comparison of the firn model with in-situ firn core measurements will be presented. Then, emergence velocities calculated from each of the three methods (GPR, stake, and modelled) will be compared. Distributed geodetic mass balances are then calculated using two approaches for constraining firn compaction and ice emergence. Geodetic mass balances are then compared to in-situ measurements from mass balance stakes and GPR, mass balance elevation profiles, and glacier-wide average mass balances.

5.1 Firn Model

The firn model was optimized to fit three end-of-summer firn cores collected from the accumulation zone of Wolverine Glacier (Figure 7). Varying values for the tuning factor f and minimum density increase were tested to minimize the RMSE between observed and modelled densities. The modelled and in-situ densities were compared by binning the measured core densities within the same layer depths as defined by the model. Optimized values of $f = 1610$ and a minimum density increase of 20 kg/m^3 were found, with a RMSE of 34 kg/m^3. These differed from parameters used in Huss (2013), which were $f = 1380$ and a minimum density increase of 10 kg/m^3, reflecting the climatic variables that are observed at Wolverine Glacier. Interannual variability in firn compaction was significant over the 2001–2020 time period (Figure 8) with values ranging between 1.78 to 2.59 m at the highest elevations (1600 m) and 0.28 to 0.94 m at lower elevations (1300 m). In general, years with greater magnitudes of firn compaction immediately followed years of above average glacier wide annual mass balances.

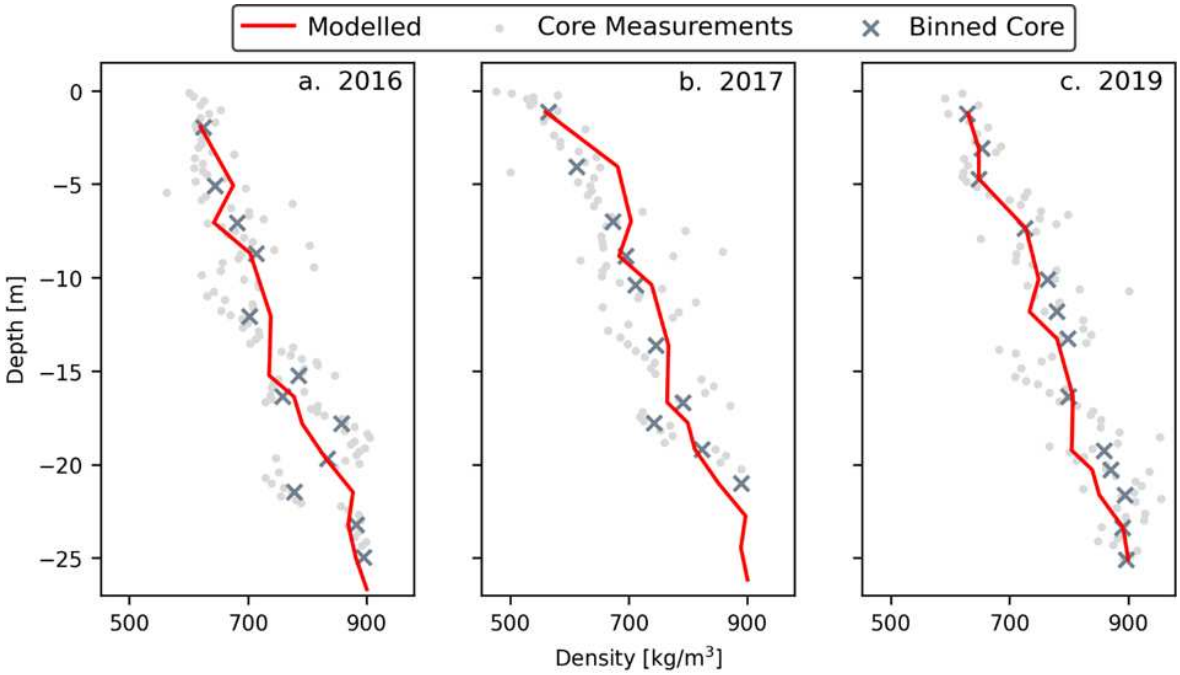

Figure 7: Comparison of densities from the firn model and three firn cores using the optimized parameters. Red lines show modelled densities, grey X's show core densities binned within the same depths as the modelled layers, and light grey dots show all individual core density measurements.

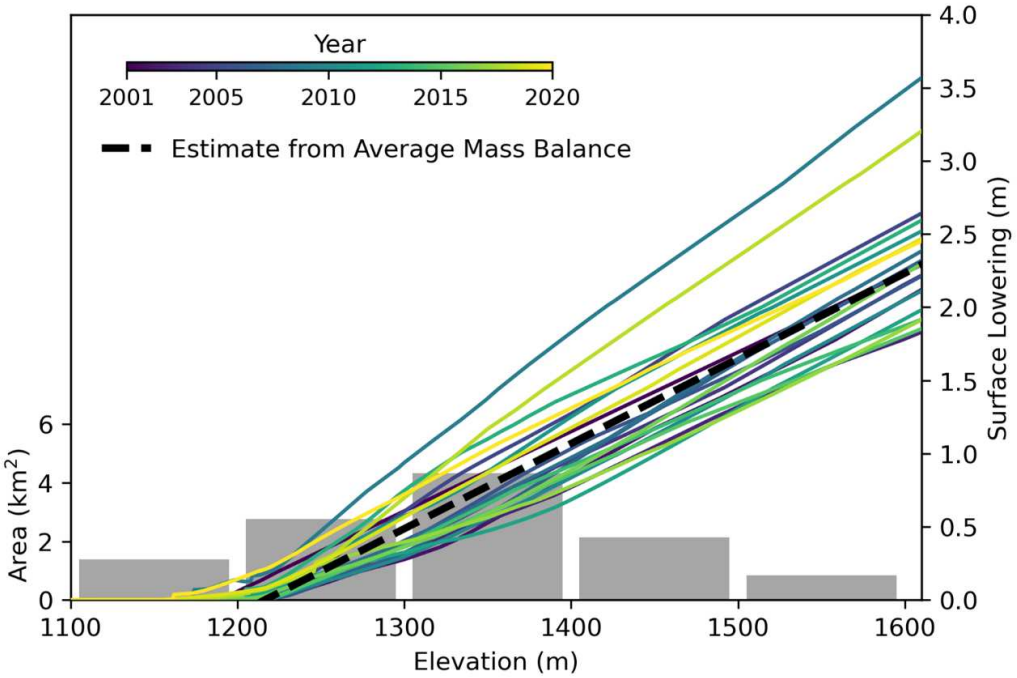

Figure 8: Elevation profiles of surface lowering due to firn compaction in each of the past 20 years (2001 to 2020) are shown. Dashed black line shows expected firn surface lowering calculated from the modelling approach using the average mass balance over the 20-year time period, as described in Sold et al. (2013). Dark grey bars show the distribution of glacier surface area within 100 m contours (left axis).

5.2 Emergence Velocities

Results from each of the three methods for measuring emergence velocities (GPR, stake, and modelling approaches) will be presented below.

5.2.1 GPR Emergence

Inputs for the GPR emergence calculations for each of the three years (elevation change, snow depths, and firn compaction) varied, but the resulting emergence velocities showed similar distributions and magnitudes (Figure 9). Average glacier-wide elevation change ranged from +4.27 meters (2017) to +6.80 meters (2016). Average snow depths ranging from 4.66 meters (2017) to 7.75 meters (2016). The extent of firn varied slightly from year to year as a result of varying end-of-summer snow line altitudes in the previous years. The total firn area ranged from 9.02 km^2 (2020) to 9.15 km^2 (2017), and average firn lowering in the accumulation zone ranged from 0.57 meters (2020) to 1.03 meters (2017). Values for elevation change due to ice melt and temporal alignment of GPR and spring DEM surveys are presented separately in Figure 10. Vertical calibrations applied to the winter DEM (to observe mass continuity) were –0.10, –0.54, and +1.17 meters (2016, 2017, and 2020, respectively).

Emergence velocities follow the expected pattern of positive values (emergence) in the ablation zone and negative (submergence) in the accumulation zone. Elevation profiles of emergence velocities in each year are very similar, with an interannual range of less than 1.41 m/yr across 87% of the glacier area (elevation above 1000 m) (Figure 11).

Minimum velocities in each year (the highest magnitude of submergence) were –4 m/yr in the upper accumulation zone in each year, and maximum velocities (highest magnitude of emergence) ranged from +4 to +7 m/yr approximately 1 km from the terminus (700 m elevation).

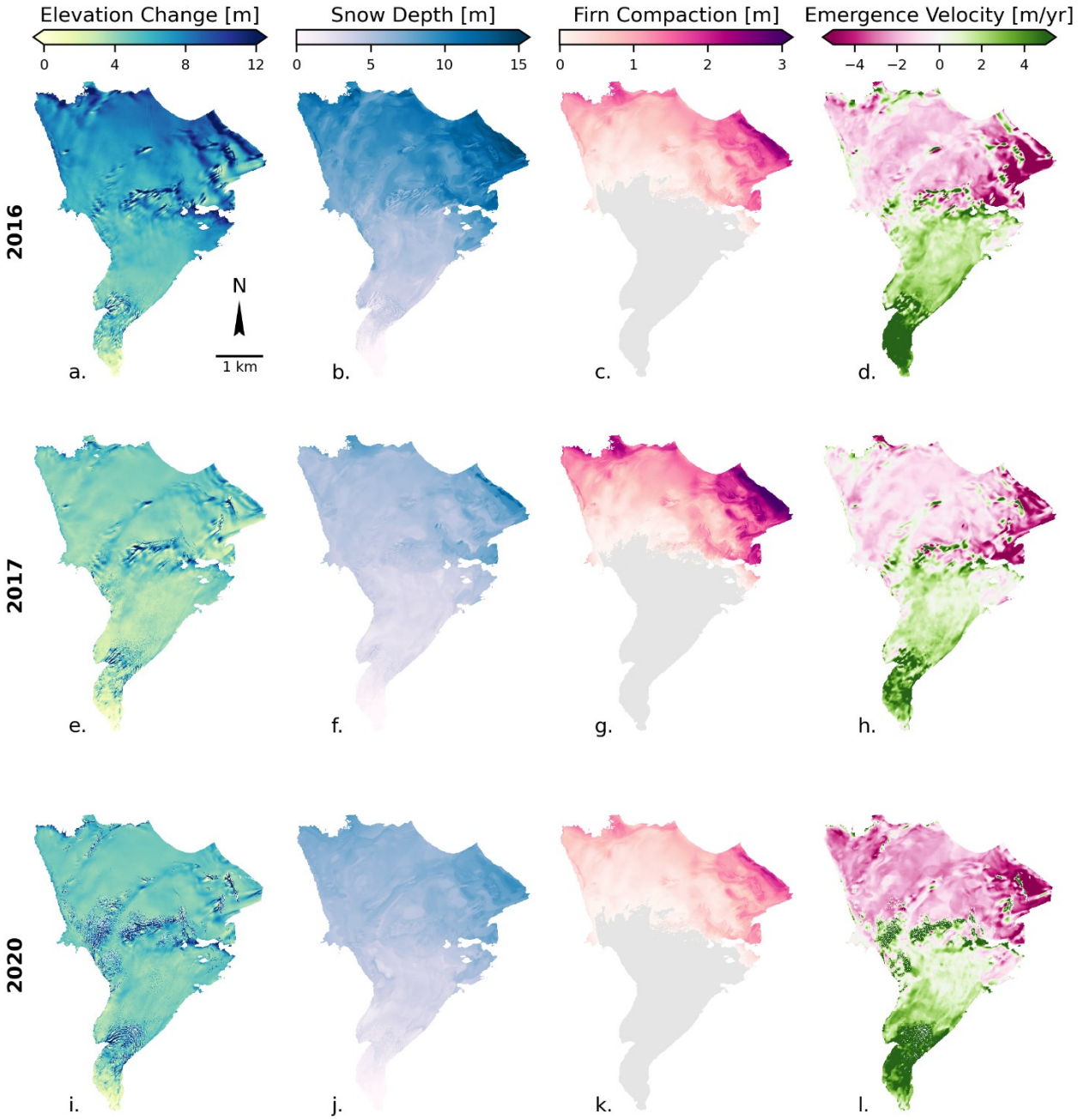

Figure 9: Inputs for GPR emergence velocity calculation over each of the three winters (a-c, e-g, i-k) and the resulting distributed emergence velocities (d, h, l). Note that additional inputs used to temporally align the DEMs and snow depth products (from mass balance model) and winter melt are not shown (see Fig. S1).

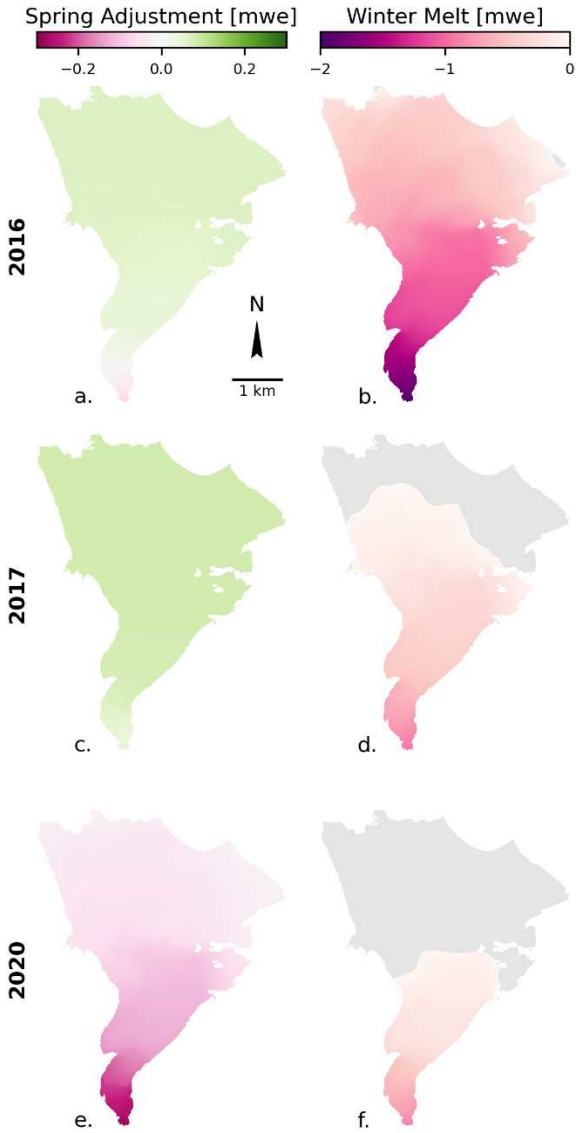

Figure 10: Surface change due to temporal alignment of GPR and spring DEM surveys (a, c, e) and winter melt occurring after the DEM capture (b, d, f) in each of the three years. These were used as additional inputs in the calculation of GPR emergence velocities.

Emergence velocities decreased rapidly in each year over the short distance between the point of maximum emergence and the terminus. The mean elevation of zero emergence is at 1207 m elevation (ranging from 1199 to 1219 m), near the 20-year average ELA of 1226 meters as expected. The largest inter-annual differences occur near the terminus of the glacier and represent only a very small fraction of the glacier area.

Small scale spatial variations in the observed emergence velocities are likely due to a combination of real variations in emergence due to complex patterns of ice flow as well as artifacts from the methodology (i.e. inaccurate snow depths or advecting topography).

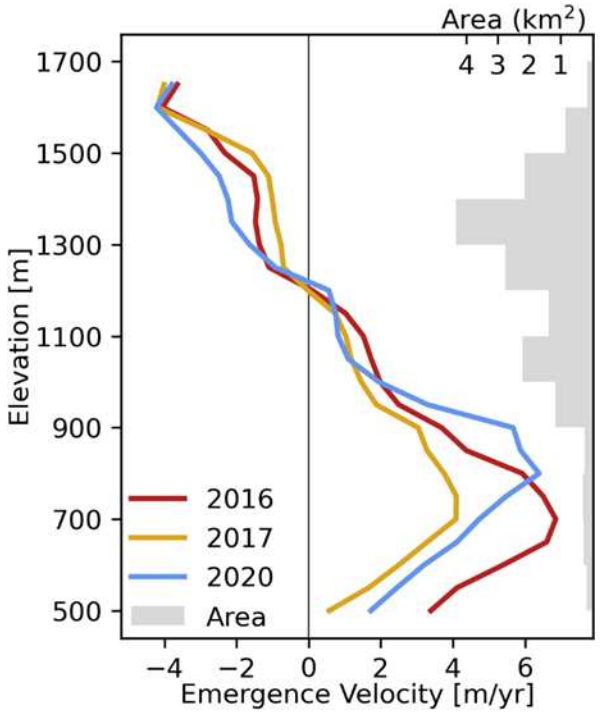

Figure 11: Elevation profiles of GPR emergence velocities in each year displayed as the median value in 50 m elevation bands. Grey bars (right y-axis) show the distribution of glacier surface area within 100 m elevation bands.

5.2.2 Stake Emergence

Point observations of emergence velocities as calculated from GNSS measurements of mass balance stakes showed a similar elevation dependence as the GPR emergence measurements (Figure 12 & Figure 16). Large variations in velocities were found for most stakes in both the modern (2015–2019) and historical (1975–1995) datasets. The stake closest to the terminus (~600 m elevation) in each dataset showed the largest variation, with a range of 20 m/yr between individual measurements for the historical dataset and 5 m/yr for the modern stake. The higher elevation stakes in the historical dataset showed a range of 6 m/yr and 5 m/yr, while

higher elevation stakes in the modern dataset generally showed less variation, with ranges of less than 3 m/yr other than at stake C (~1300 m elevation) which had a range of 6 m/yr.

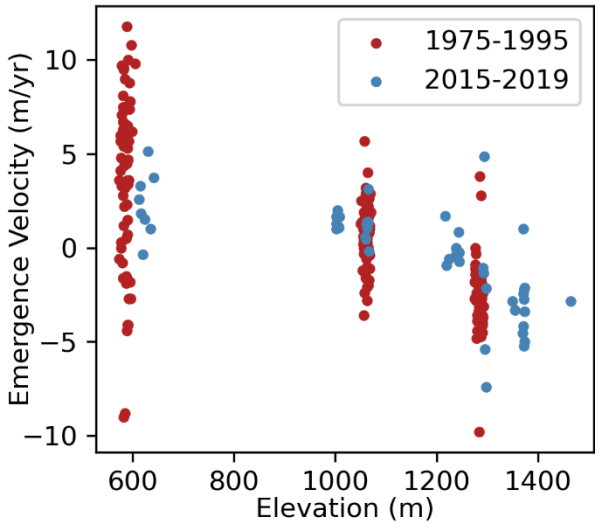

Figure 12: The distribution of emergence velocities calculated from repeat GNSS measurements of mass balance stakes, plotted according to elevation of the stake. Red shows measurements from historical stakes (1975-1995), and blue shows measurements from modern stakes (2015-2019).

Stake locations in the historical dataset were measured three times per year (in September, January, and May/June), while modern stakes are measured only twice (in September and May). The greater sample size provided by the historical dataset (both from the number of years represented and measurement frequency) allowed the seasonality of emergence and horizontal velocities to be investigated (Figure 12; Figure 13). A distinct seasonality was observed at stake A (closest to the terminus), with velocities ranging from –1.5 m/yr in mid-August to +8.8 m/yr in mid-February. Seasonality at the two other stakes was less discernible, with variations of ±0.5 and 0.7 m/yr at stakes B and C (elevations 1050 and 1275 m respectively).

Further discussion of the possible causes of the large variation in stake emergence velocities can be found in Section 6: Uncertainties.

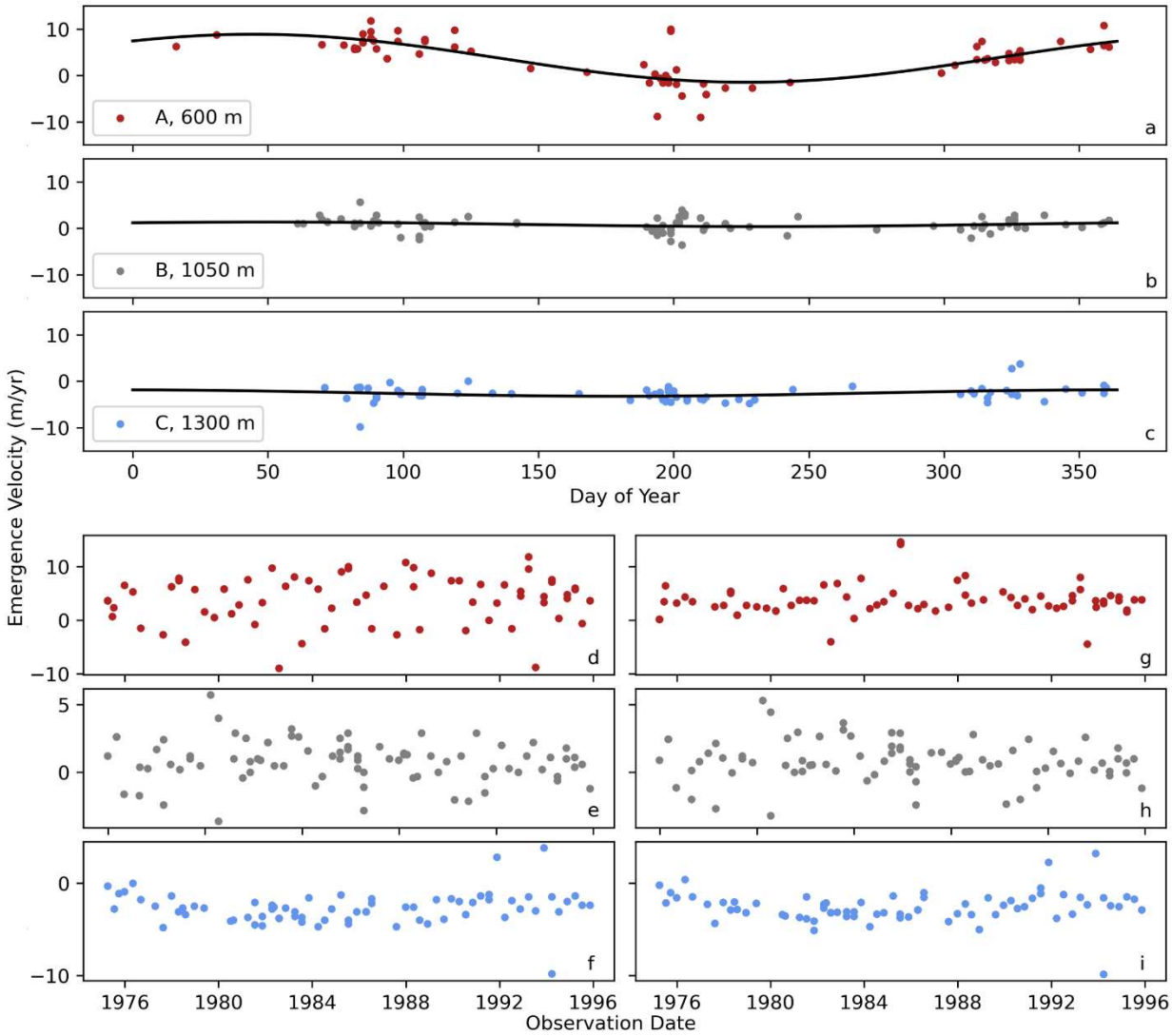

Figure 13: Seasonality of emergence velocity observed in the old stake measurements. Stake A (red) is the lowest elevation stake near the terminus, stake B (grey) is near the ELA, and stake C (blue) is the highest elevation in the accumulation zone. Top figure shows a best-fit sine curve for each stake data, with each point representing a single emergence measurement plotted by the day of year on the x-axis (middle date between the two stake measurements) and emergence velocity on y-axis. Bottom left shows the time series of stake emergence from 1975 to 1995, and bottom right shows the time series but corrected for the seasonal variation calculated by the sine curve fit. Seasonality in velocities is clearly visible in stake A, while not as obvious in stakes B and C.

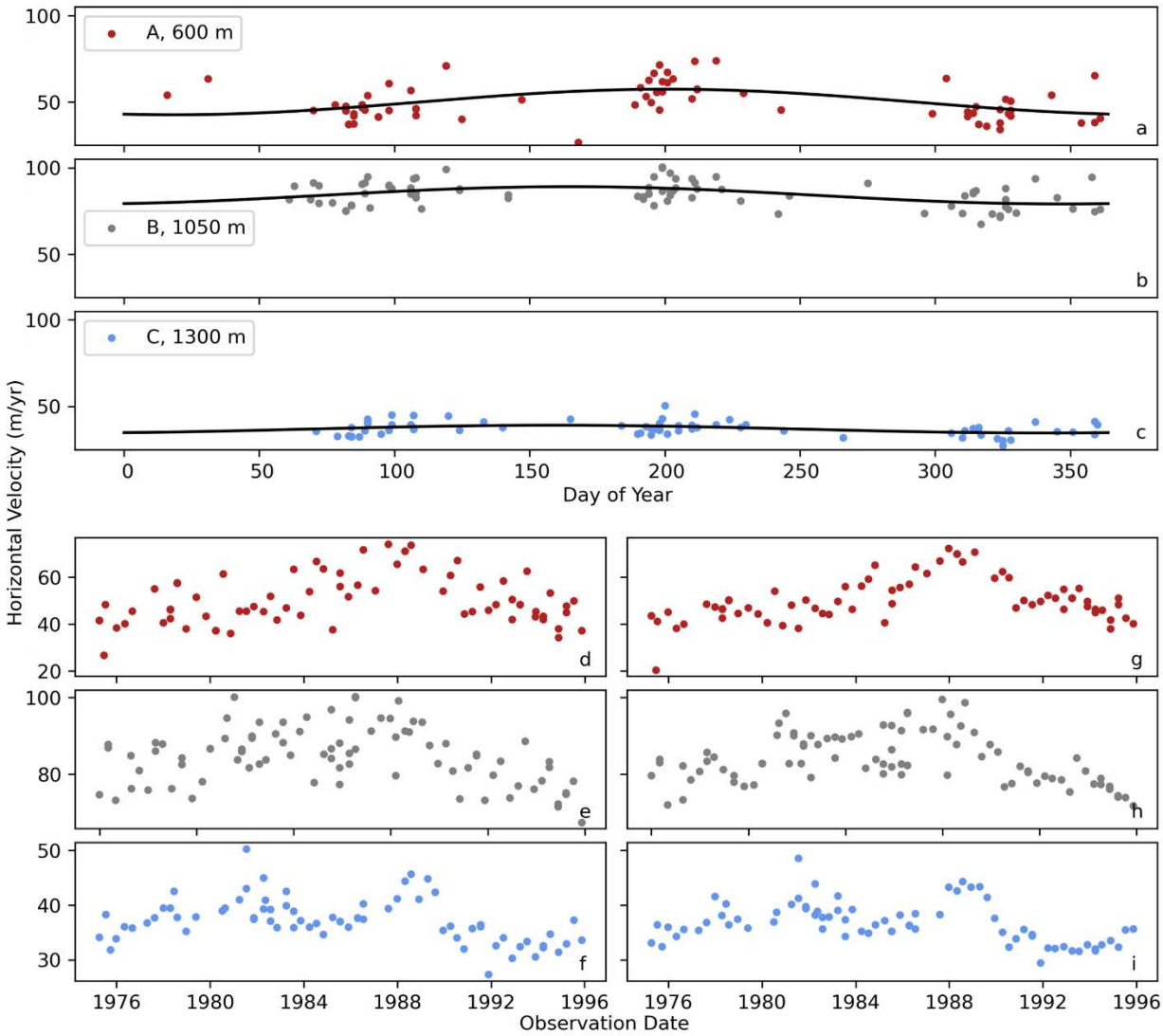

Figure 14: Like Fig. 13, but for horizontal velocities. Similar to emergence velocities, the seasonality is more pronounced in stake A than stakes B or C.

5.2.3 Modelled Emergence

Mass balance modelled emergence velocities were calculated for four intervals based on DEM availability: 2015–2019, 2008–2012, 1972–1979, and 1972–1995. The 2015–2019 interval aligns with the GPR emergence velocity calculations and modern stake emergence observations. The 1972–1995 interval aligns with historical stake emergence observations. The 2008–2012 and

1972–1979 interval offer the opportunity to test the methodology on shorter temporal scales similar to the 2015–2019 interval. Results from 2015–2019 and 1972–1995 are shown in Figure 16. Elevation profiles for all four intervals are presented in Figure 15.

Emergence velocities in all four intervals followed the general pattern of submergence in the accumulation zone and emergence in the ablation zone, with zero emergence near the ELA (ranging from 1238 m to 1270 m). Minimum values ranged from –5.0 to –3.7 m/yr, and maximum values ranged from +3.9 to +6.3 m/yr. Over 87% of the glacier area (elevations above 1000 m) the range of emergence velocities between intervals is less than 1.0 m/yr.

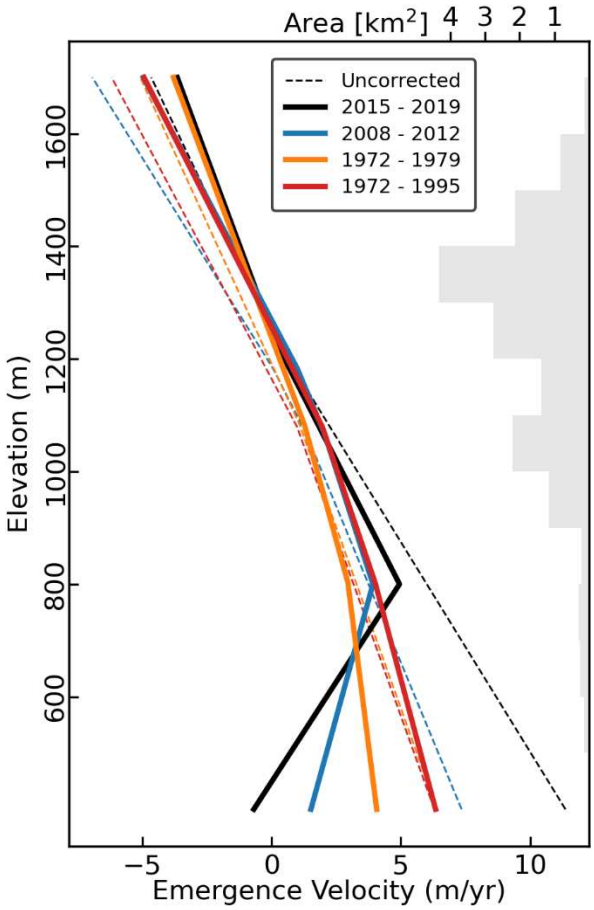

Figure 15: Mass-balance modelled emergence velocities calculated over different timeframes. Dashed lines are uncorrected for glacier thinning, and thick lines are corrected for thinning and with a constant value added such that glacier-wide emergence is equal to zero. Years 2015–19 correspond to the geodetic and modern stake measurements, years 1972–95 correspond to the historical stake measurements.

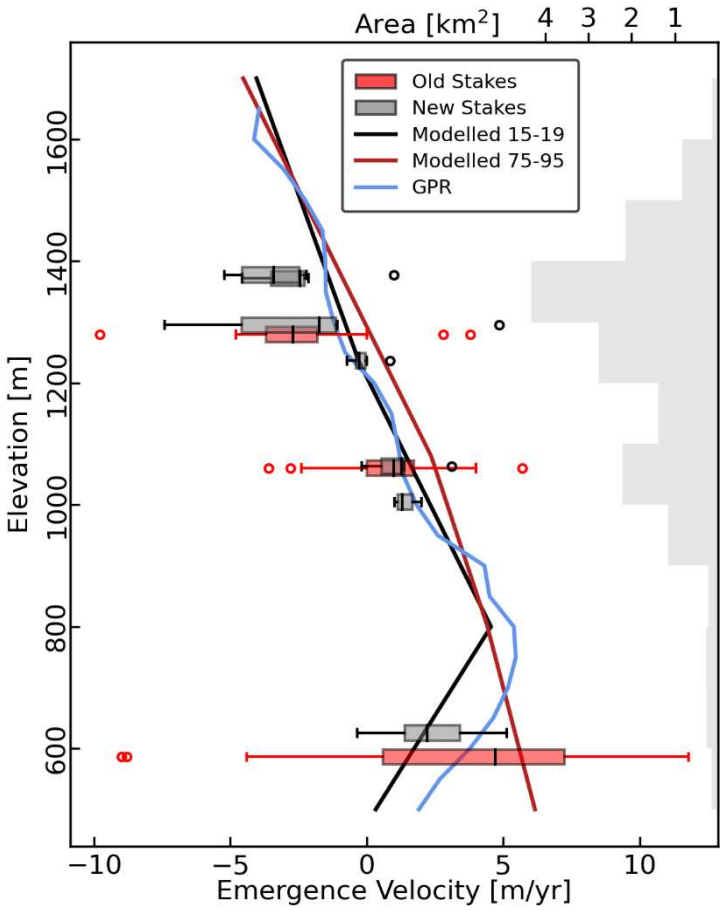

Figure 16: Comparison of the three methods of emergence velocity calculation. Boxplots correspond to the stake method; red and black lines show the modelled method over two timeframes corresponding to the 'old' and 'new' stakes; blue line shows the median GPR emergence velocity within 50 m elevation bands.

Emergence velocities from the two oldest intervals (1972–1995 and 1972–1979) continued to increase at lower elevations near the terminus. In the two most recent intervals (2008–2012 and 2015–2019) the emergence velocities decreased at the lowest elevations near the terminus, in a pattern similar to the GPR emergence products. This decrease is more pronounced in the 2015–2019 interval, where emergence velocities are near zero at the terminus. The locations of the inflection point (800 meters) in these intervals is a function of the piecewise linear fit that was used to account for glacier thinning and captures only the general pattern of

emergence in these locations (Figure 6). In reality, the emergence velocities in this zone should show a more gradual inflection (as seen in the GPR emergence).

Glacier-wide emergence adjustments to follow mass continuity ranged from +0.02 m/yr to +1.44 m/yr. These adjustments are necessary because the mass balance profiles used to model emergence velocities tend to over-estimate glacier wide mass balance (O'Neel et al., 2019).

5.3 Geodetic Mass Balance Measurements

Distributed geodetic mass balance was measured geodetically for six time periods using two approaches for constraining the effects of ice emergence and firn compaction: 1) using the GPR emergence velocities and fully distributed firn compaction, and 2) using the modelled emergence velocities and elevation-dependent firn compaction (i.e. not considering spatial variability in firn compaction within elevation bands). Approach 1 will be referred to as the distributed method and approach 2 will be referred to as the profile method.

To avoid circular reasoning in the distributed mass balance measurements, GPR-derived emergence velocities were not used during the years in which they were collected. For example, in the 2016 winter and annual mass balance measurements the average emergence velocities from 2017 and 2020 are used (calculated as the pixel-wise mean). For the 2019 annual mass balance the data from all three years is used.

Both methods give reasonable distributions and magnitudes of mass balance in all six time periods (Figure 17 & Figure 18), showing strong elevation-dependent trends along with elevation-independent spatial variability. These patterns of spatial variability are consistent

across different years and align with end-of-summer distributions of firn and ice (areas of lower annual mass balance) observed in the accumulation zone (Figure 19).

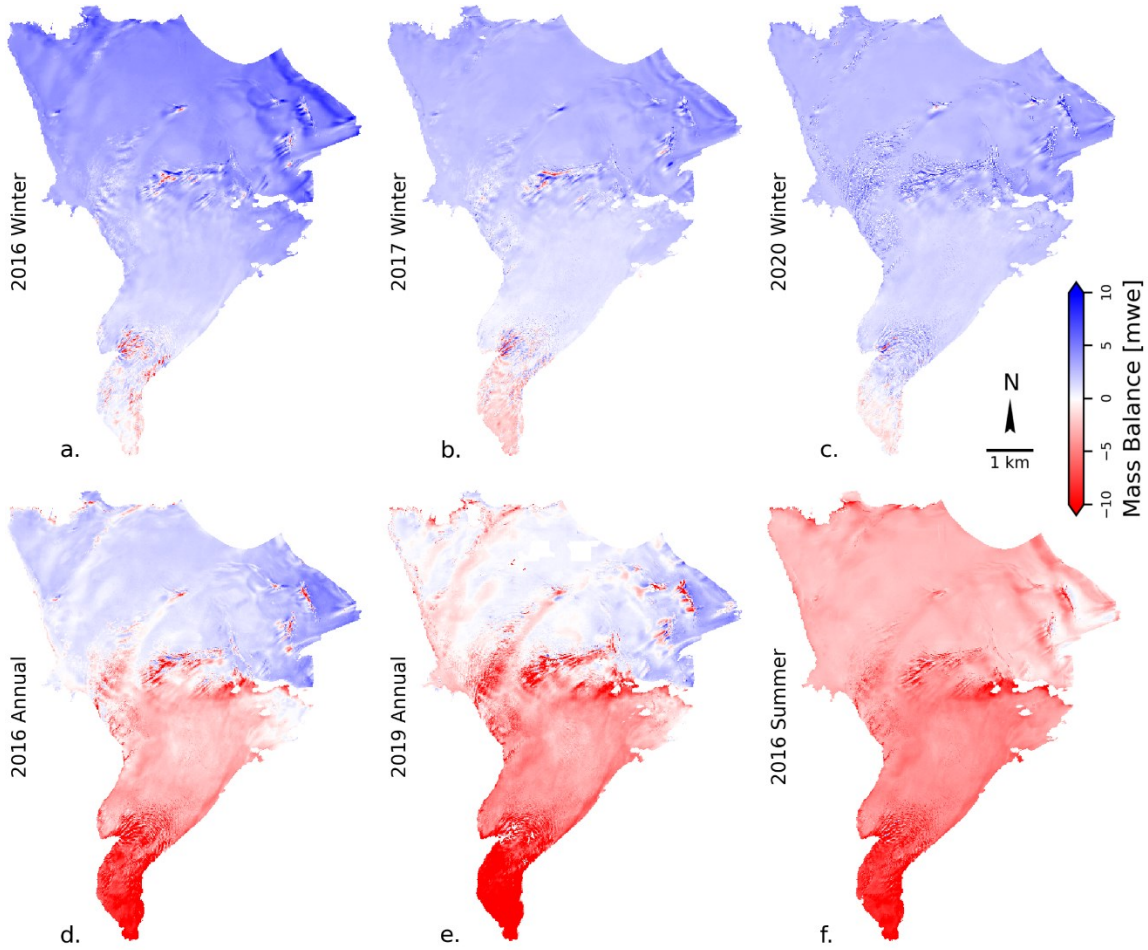

Figure 17: Geodetic mass balance measurements over six time periods, calculated using the distributed approach.

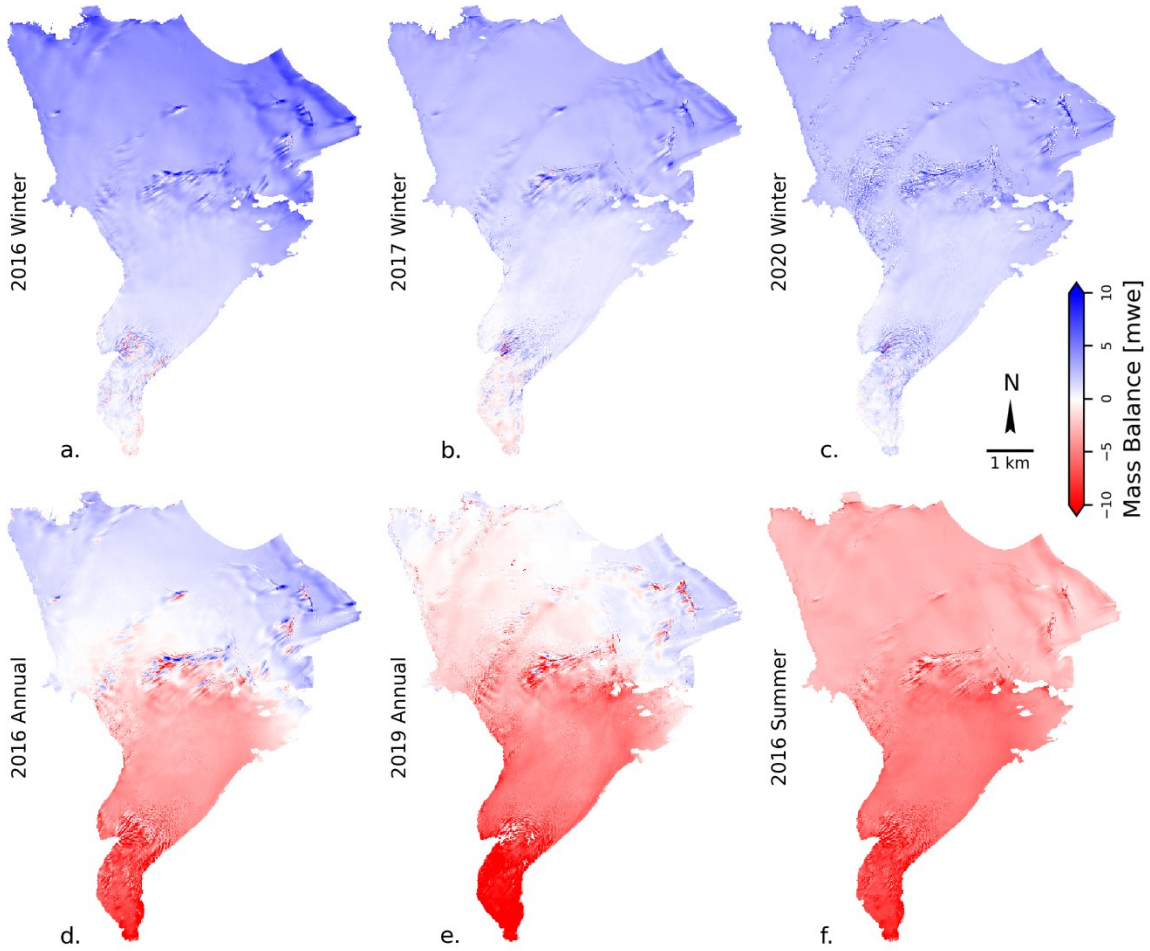

Figure 18: Geodetic mass balance measurements over six time periods, calculated using the profile approach.

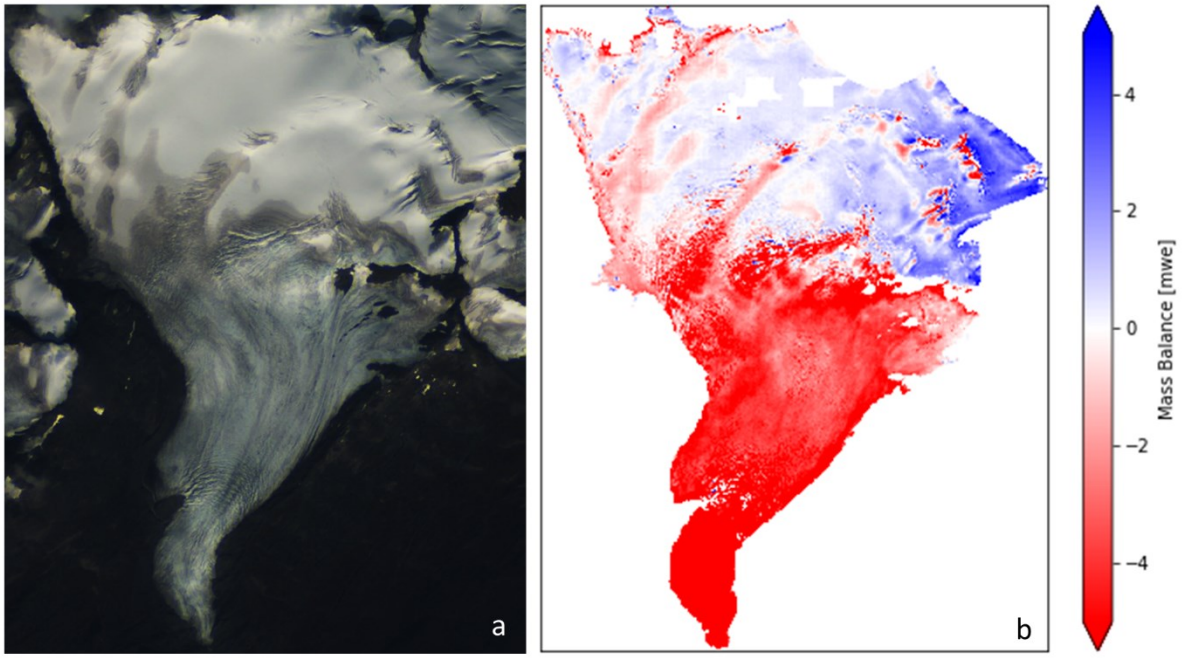

Figure 19: a) Sentinel-2 satellite image of Wolverine Glacier near the end of summer 2019 (September 14, 2019), coincident with the 2019 Fall DEM. The raster values have been stretched to enhance identification of snow (lightest areas in the northern section), firn (grey areas between snow and ice), and ice (dark grey/blue). b) 2019 distributed annual mass balance as calculated in this study, with the colorbar limits condensed to highlight the boundaries between areas of positive and negative mass balance. The distribution of surface types in the Sentinel-2 image matches with the distribution of mass gain and loss, with areas of mass gain coinciding with snow surfaces, and areas of mass loss coinciding with areas of firn and snow. This indicates that the geodetic mass balance measurement captured some of the elevation-independent variability in mass balance processes.

5.4 Geodetic – Stake Balance Comparison

In-situ measurements from mass balance stakes were compared to point geodetic mass balance measurements at stake locations, using the mass balance model to temporally align measurements (Figure 20). A total of 41 in-situ stake measurements were used, distributed across the glacier surface and across all five timeframes (Table 1). The distributed balance method gave more accurate results than the profile method. The distributed balance method had an RMSE of 0.55 m w.e. and mean bias of –0.18 m w.e. (indicating a geodetic over-estimation of 0.18 m w.e.), while the profile method had an RMSE of 0.68 m w.e. and bias of –0.40 m w.e. Results

tended to be more accurate in the winter and summer seasons than over annual timeframes (Table 3).

Table 3: RMSE and mean bias (stake minus geodetic) for the comparison between geodetic and stake mass balance measurements (Figure 20), using both distributed and profile geodetic approaches. "Obs" indicates the number of stake measurements for each time period.

	Distributed		**Profile**		
	RMSE	Bias	RMSE	Bias	Obs
Overall	0.55	–0.18	0.68	–0.40	41
Winter	0.50	–0.11	0.53	–0.21	20
Summer	0.55	+0.05	0.43	–0.17	7
Annual	0.63	–0.38	0.93	–0.79	14

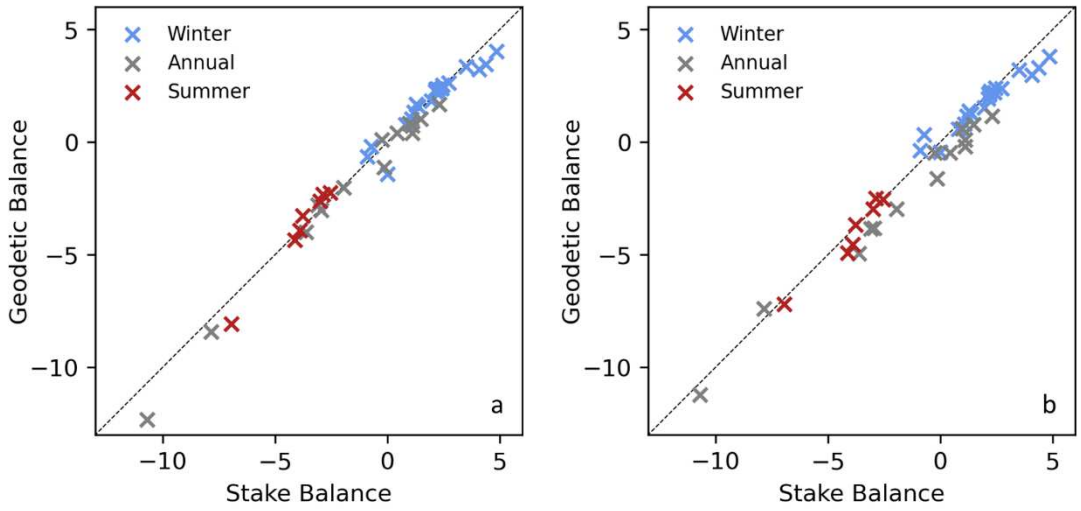

Figure 20: Comparison of in-situ mass balance measurements from stakes and geodetic mass balance measurements at the same points. (a) showing the geodetic mass balance measured using the distributed approach, and (b) showing results from the profile approach.

5.5 Geodetic – GPR Balance Comparison

Over each of the three winter seasons, geodetic mass balance measurements were compared to GPR-derived snow depths, allowing comparisons at 1700 to 4000 locations per year. The mass balance model was used to temporally align the two datasets.

Using the distributed method for constraining ice emergence and firn compaction, RMSE values ranged from 0.32 to 0.43 m w.e. (2020 and 2017, respectively), and the bias ranged from -0.001 to +0.26 m w.e (2020 and 2017) (Table 4). The spatial distribution of accuracy did not show a consistent pattern across all years (Figure 21). In 2016, the geodetic mass balance estimates were slightly more accurate and less biased in the accumulation zone than the ablation zone. However, in 2017 the pattern was reversed, with less accuracy and greater bias in the accumulation zone. In 2020, there were not sufficient GPR observations at higher elevations to allow such a comparison. In all years, the greatest differences between geodetic and GPR mass balance measurements were near the edges of the glacier or in heavily crevassed areas.

Using the profile method for constraining ice emergence and firn compaction largely outperformed the distributed approach in 2016 and 2017, giving smaller RMSE values and lower magnitudes of bias across the entire glacier surface, in the accumulation zone in both years, and in the ablation zone in 2016 (Figure 21, Table 4). In 2020, the profile approach tended to underestimate the mass balance along GPR tracks surveyed, giving a higher RMSE and magnitude of bias compared to the GPR emergence method.

Table 4: Statistics for the geodetic-GPR mass balance comparisons (Figure 21) showing the mean bias (geodetic minus GPR) and the RMSE of the differences over the entire glacier surface as well as for only the accumulation and ablation zones. Obs refers to the number of 10x10 m grid cells observed each year.

	Distributed Method						**Profile Method**						
	Entire Glacier		Accumulation		Ablation		Entire Glacier		Accumulation		Ablation		
Year	Bias	RMSE	Bias	RMSE	Bias	RMSE	Bias	RMSE	Bias	RMSE	Bias	RMSE	Obs
2016	0.10	0.34	0.07	0.30	0.17	0.43	-0.03	0.31	-0.06	0.29	0.05	0.37	3192
2017	0.26	0.43	0.36	0.50	0.11	0.28	0.08	0.29	0.17	0.29	-0.05	0.38	4096
2020	0.00	0.32	-0.10	0.48	0.01	0.30	-0.22	0.40	-0.23	0.54	-0.22	0.38	1737

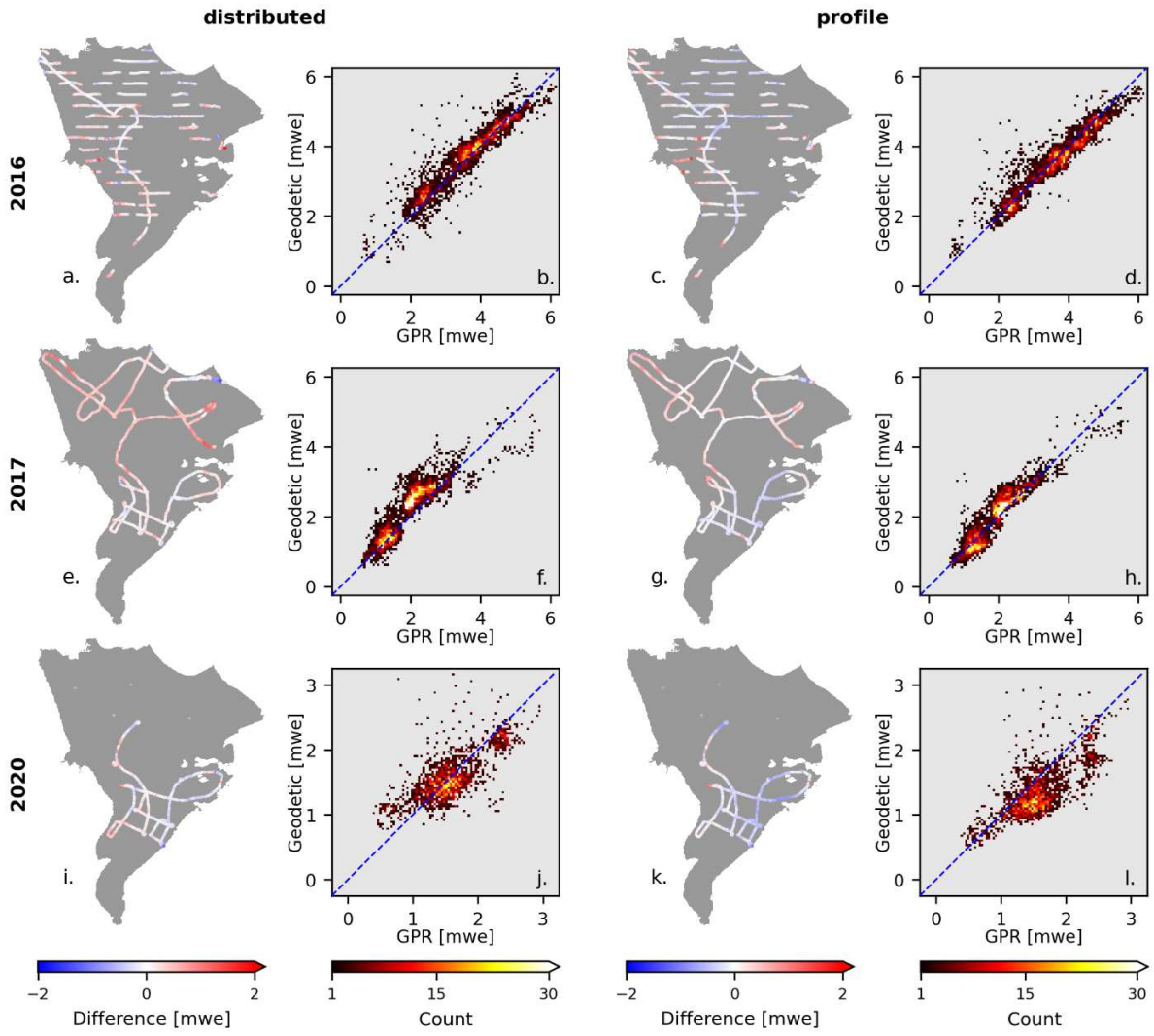

Figure 21: Comparison of GPR mass balances with geodetic winter mass balances derived using the distributed method (a,b,e,f,i,j) and profile method (c,d,g,h,k,l) in each of the three winter seasons investigated (as shown by the year labels on the left). Maps display the spatial distribution of differences (geodetic minus GPR). Scatterplots compare the mass balances at each point to each other, displayed as a heatmap. Dashed blue lines in indicate the line of perfect agreement between the two datasets. Note different axes limits for plots j and 1.

5.6 Mass Balance Profile Comparison

Elevation profiles of mass balance (balance profiles) were calculated for the geodetic mass balance measurements, using both distributed and profile approaches (Figure 22). The mean geodetic mass balance was calculated for each 100-meter elevation band on the glacier

surface. Balance profiles using mass balance stake observations are calculated for each summer, winter, and annual balance period by using a piecewise-linear fit to all available stake data (n=8) (O'Neel et al., 2019). These stake-derived balance profiles are used for glacier-wide mass balance calculations on Wolverine Glacier, as well as numerous other glaciers globally. The mass balance model was used to temporally align geodetic observations to the floating-date time system used in the stake-derived profiles.

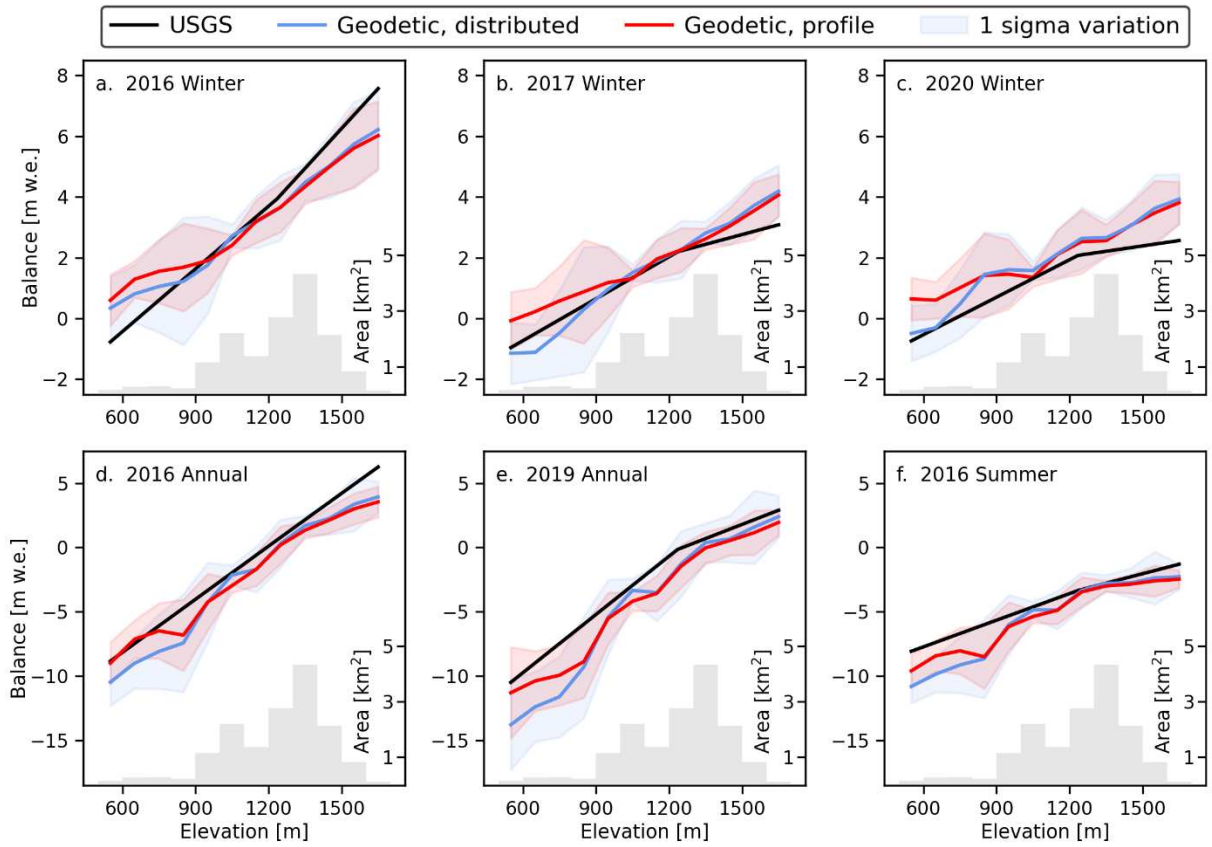

Figure 22: Mass balance profiles from USGS stake data (black lines), distributed geodetic balance (blue lines), and geodetic profiles (red lines) plotted by mean pixel value in 100 m elevation bands. Filled areas indicate one standard deviation from the mean in each elevation band from each of the geodetic products (blue and red areas). Note different axes for a-c and d-f.

Balance profiles from GPR and modelled emergence velocities show good agreement over the majority of the glacier surface, diverging most in the bottom 300 to 400 meters near the

terminus and at the very highest elevation bands (Figure 22). The distributed balances were more negative in all six time periods at the terminus, due to higher magnitude emergence velocities in this area (Figure 16). Stake-derived balance profiles showed more consistent differences. In all annual and summer intervals the stake profiles showed more positive mass balances over the vast majority of the glacier surface. In 2020 winter, the stake profile was lower across all elevation bands, with greater differences at the highest elevations. In 2016 and 2017 winter the stake balance profiles were most different at the highest and lowest elevations. In 2016 winter, the stake profile estimated higher mass balance than geodetic profiles in the accumulation zone, while the 2017 winter stake balance profile estimated lower mass balance in the accumulation zone.

5.7 Glacier-wide Mass Balance Comparison

Glacier-wide geodetic mass balance averages for each time period were calculated for comparison to USGS-derived values (Figure 23, Table 5). USGS glacier-wide balances are calculated by applying stake-derive profiles over the entire glacier surface, and then applying a systematic geodetic calibration (O'Neel et al., 2019). The two geodetic approaches gave very similar results, with maximum differences of 0.064 m w.e. in the winter seasons and 0.23 m w.e. over annual time periods. The profile approach gave lower mass balances in all time periods.

Differences between geodetic and USGS-derived balances were overall greater. The 2017 and 2020 winter USGS balances were ~0.6 and 0.9 m w.e. lower than geodetic mass balances. The 2016 winter USGS balance was very similar to geodetic measurements, with differences of <0.01 and 0.05 m w.e.. Annual USGS mass balances were slightly more positive than geodetic

measurements, with differences ranging from 0.02 m w.e. to 0.5 m w.e.. The summer 2016 geodetic and USGS mass balances were very similar, with differences of 0.03 and 0.17 m w.e..

Without the geodetic calibration that was applied to the USGS annual and summer mass balances, the differences increase by 0.68 m w.e. (a calibration of –0.68 m w.e. was used for all years in this time period).

Table 5: Glacier-wide mass balance values (m w.e.) from Figure 23

Method	2016 Winter	2017 Winter	2020 Winter	2016 Annual	2019 Annual	2016 Summer
Distributed	3.75	2.25	2.37	-0.16	-1.76	-3.91
Profile	3.69	2.22	2.30	-0.36	-2.00	-4.05
USGS	3.74	1.64	1.47	-0.14	-1.50	-3.88
USGS, uncalibrated	---	---	---	0.54	-0.82	-3.2

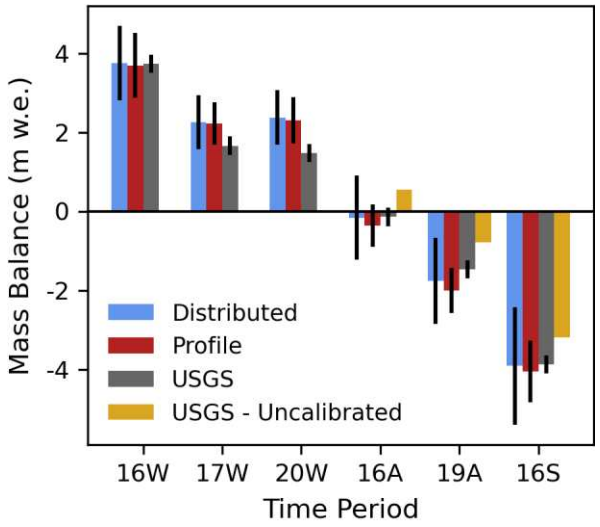

Figure 23: Glacier-wide geodetic balances, using both distributed and mass-balance modelled emergence, compared to USGS glacier-wide balances, temporally aligned using the mass balance model. Yellow bars indicate the USGS mass balance for each annual and summer period without a geodetic calibration applied. Black lines show the estimated uncertainty.

6. UNCERTAINTY ASSESSMENT

6.1 GPR Uncertainties

McGrath et al. (2015) estimated an uncertainty of ±17% in point SWE values along GPR tracks (with part of the uncertainty related to the snow depth to SWE conversion). Sold et al. (2013) estimated uncertainty in snow depths along GPR track to be ±5% in dry conditions, with an additional –13% possible depending on liquid water content in the snowpack. An uncertainty of 10% is assumed for snow depths along GPR track here. Uncertainties related to the extrapolation of snow depths across the glacier surface are difficult to quantify and are likely to be large in areas of the glacier that are under sampled. As such, the off-track snow depths, GPR emergence velocities, and geodetic mass balance estimates have higher uncertainties than the same values along-track.

6.2 DEM Alignment Uncertainties

Vertical uncertainty related to the vertical alignment of summer DEMs ($\sigma_{\Delta z}$) is calculated as the median absolute deviation of the elevation difference in off-glacier terrain, multiplied by 1.4826 (O'Neel et al., 2019) (Table 6). Only relative accuracy (between pairs DEMs) is needed for these analyses, so absolute accuracy of individual DEMs is not quantified.

Uncertainties are calculated using DEMs in their original resolution (ranging from 0.5 m to 5 m) rather than when resampled to 10 m. These values are used to calculate uncertainty related to thinning rate (Section 6.7). Histograms showing the distribution of the elevation difference in off-glacier terrain during each time period can be found in Figure 1Figure 24.

The limited snow free area in winter DEMs makes estimating uncertainty in the vertical co-registration of these products difficult. Therefore, an uncertainty of ±1.0 m is assumed for all seasonal and annual alignments.

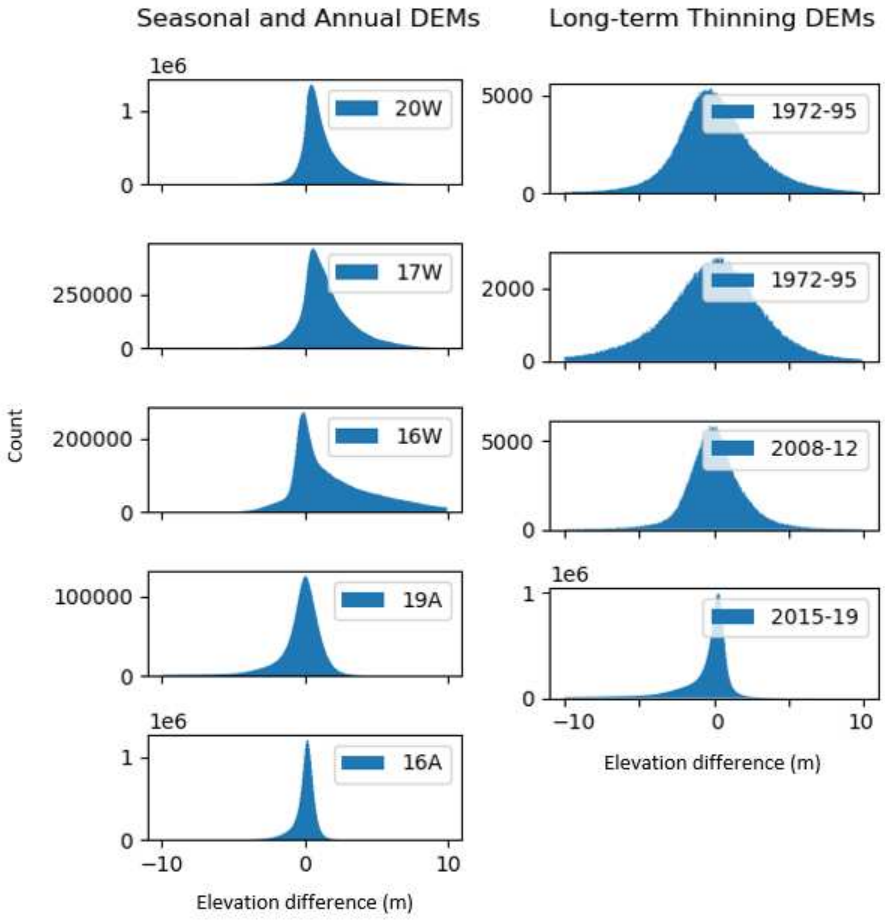

Figure 24: Elevation difference in off-glacier, stable terrain pixels. In the left column is the difference in DEMs corresponding to the three winter and two annual time period used for distributed geodetic mass balances. On the right is the difference in DEMs corresponding to intervals over which long-term thinning rates were calculated. The positive skew in the three winter seasons shows the effect of near-complete snow cover on the off-glacier terrain. Negative skew in the 19A and 2015–19 periods shows the varying effect of vegetation on DEMs derived from lidar (which can see through vegetation) and SfM (which cannot).

Table 6: Uncertainties related to DEM vertical alignment when stable, snow-free ground is present

Timeframe	M.A.D. (m)	Years	Thinning Rate Uncertainty (m/yr)
2015–16	0.49	1	NaN
2018–19	1.07	1	NaN
1972–95	2.37	23	0.10
1972–79	3.08	7	0.44
2008–12	1.61	4	0.40
2015–19	0.84	4	0.21

6.3 Mass Balance Model Uncertainties

Glacier-wide average adjustments ranged from –0.19 to +0.576 m w.e. over all intervals for which it was used. An uncertainty of ±20% of the estimated mass change is assumed for each given interval.

6.4 Firn Compaction Uncertainties

Uncertainties in the magnitude of firn compaction are difficult to quantify due to the limited research that has been conducted on temperate mountain glaciers. To account for uncertainties in temporal variations in firn compaction and distributed annual balances, an uncertainty of ±30% of the magnitude of firn compaction a given point is assumed. The choice of 30% was guided by inter-annual variations in firn compaction given by the model (Figure 8).

6.5 Stake emergence uncertainties

For both historical and modern stake datasets, uncertainty in vertical stake displacement between measurements is estimated to be ±0.2 m (following Stocker-Waldhuber et al., 2019) to allow for uncertainty in vertical GNSS positioning, stake tilt, and burrowing. An uncertainty of

±0.4 m is given for estimation of the expected elevation change (Δz_e in Eq. (6)), to allow for advecting topography and small-scale spatial variation in the flow field. Values for Δz_e in this study ranged from 0 to –6.2 m, with 90% less than 4 m. Glaciers with slower horizontal velocities will likely have smaller uncertainties. Combined via a quadratic sum, these lead to an uncertainty of ±0.45 m of emergence between stake measurements. Scaled to annual values, this gives uncertainties of ±1.22 m/yr for stakes measured 135 days apart (measuring summer emergence) and ±0.71 m/yr for stakes measured 260 days apart (measuring winter emergence).

The methodologies for emergence velocity calculations are different for each dataset, limiting our ability to directly compare the two. There is more uncertainty in the historical measurements (which were acquired using theodolites and measured relative to a local reference frame) than the recent GNSS measurements, likely accounting for some of the increased variability observed.

6.6 GPR Emergence Uncertainties

Uncertainties in GPR-derived emergence velocities (σ_{w_GPR}, Eq. (12)) are a product of uncertainties related to partitioning observed surface elevation change ($\sigma_{\Delta z}$) into surface mass balance (σ_{snow} and σ_{b_mod}), and firn compaction (σ_{firn}), to isolate the emergence component. This represents uncertainty along GPR tracks but cannot be reliably extended to the off-track areas. Comparison of the elevation profiles of emergence across the entire glacier surface (as in Figure 11) and for only the along track pixels shows no discernible difference, suggesting that the elevations captured by GPR measurements tend to be well represented. However, the lowest elevations, and icefall areas likely are not well constrained.

$$\sigma_{w\_GPR} = \sqrt{(\sigma_{snow})^2 + (\sigma_{firn})^2 + (\sigma_{\Delta z})^2 + (\sigma_{b\_mod})^2} \quad (12)$$

Increasing magnitudes of firn compaction and snow depth with elevation leads to increased uncertainty in emergence velocities at higher elevations. Average glacier-wide uncertainties were 1.34, 1.12, 1.21 m/yr in 2016, 2017, and 2020 respectively, with values typically ranging from 0.8 m/yr at the terminus to 2.1 m/yr in the upper accumulation zone.

6.7 Modelled Emergence Uncertainties

Uncertainties in the modelled emergence velocities (σ_{w_mod}, Eq. (13)) are calculated as a combination of uncertainties in the average annual balance profile (σ_b) and the thinning rate of the glacier (σ_{thin}). Additional uncertainty is added by the constant glacier-wide adjustment value that is applied to modelled emergence profiles in each interval. Glacier-wide σ_b is estimated to be ±0.23 m w.e./yr by O'Neel et al. (2019), while σ_{thin} is calculated from the DEM alignment uncertainty and listed in Table 1Table 6. This gives uncertainties ranging from ±0.27 to ±0.50 m/yr for the elevation profile of emergence velocities. This does not account for spatial variability within elevation bands, which would increase uncertainty related to point geodetic mass balance measurements.

$$\sigma_{w\_mod} = \sqrt{\left(\frac{\sigma_b}{0.9}\right)^2 + (\sigma_{thin})^2} \quad (13)$$

6.8 Geodetic Mass Balance Uncertainty

Uncertainties in geodetic mass balance (σ_{sfc}, Eq. (15)) are a result of uncertainty related to the volume change from mass balance changes ($\sigma_v \gamma$, Eq. (14)), and the uncertainty related to

the material density ($\sigma_\rho dv$) (Beedle et al., 2014). Uncertainty in the volume change is calculated as the quadratic sum of the uncertainties in measured elevation change ($\sigma_{\Delta z}$) and partitioning elevation change into emergence (σ_w) and firn compaction (σ_{firn}). This is then multiplied by the density of the material (γ) to give units of m w.e.

Uncertainty related to the material density are calculated as the uncertainty of the density conversion, σ_γ, multiplied by the volume of the mass balance change, *dv*. We assume a generous σ_γ value of ±0.1 (a unitless conversion factor) for all points, but do not attempt to account for errors in determining the material type (i.e. differentiating between areas of snow, firn, and ice).

$$\sigma_v = \sqrt{(\sigma_{\Delta z})^2 + (\sigma_{\text{w}})^2 + (\sigma_{firn})^2} \tag{14}$$

$$\sigma_{sfc} = \sqrt{(\sigma_v \gamma)^2 + (\sigma_\gamma dv)^2} \tag{15}$$

Glacier-wide average geodetic mass balance uncertainties ranged from 0.71 to 1.18 m w.e. using the *distributed* mass balance calculation method (GPR emergence velocities), and from 0.60 to 0.78 m w.e. using the *profile* mass balance calculation method (modelled emergence velocities). Distributed uncertainties in mass balance calculations, using GPR-derived emergence velocities are shown in Figure 25.

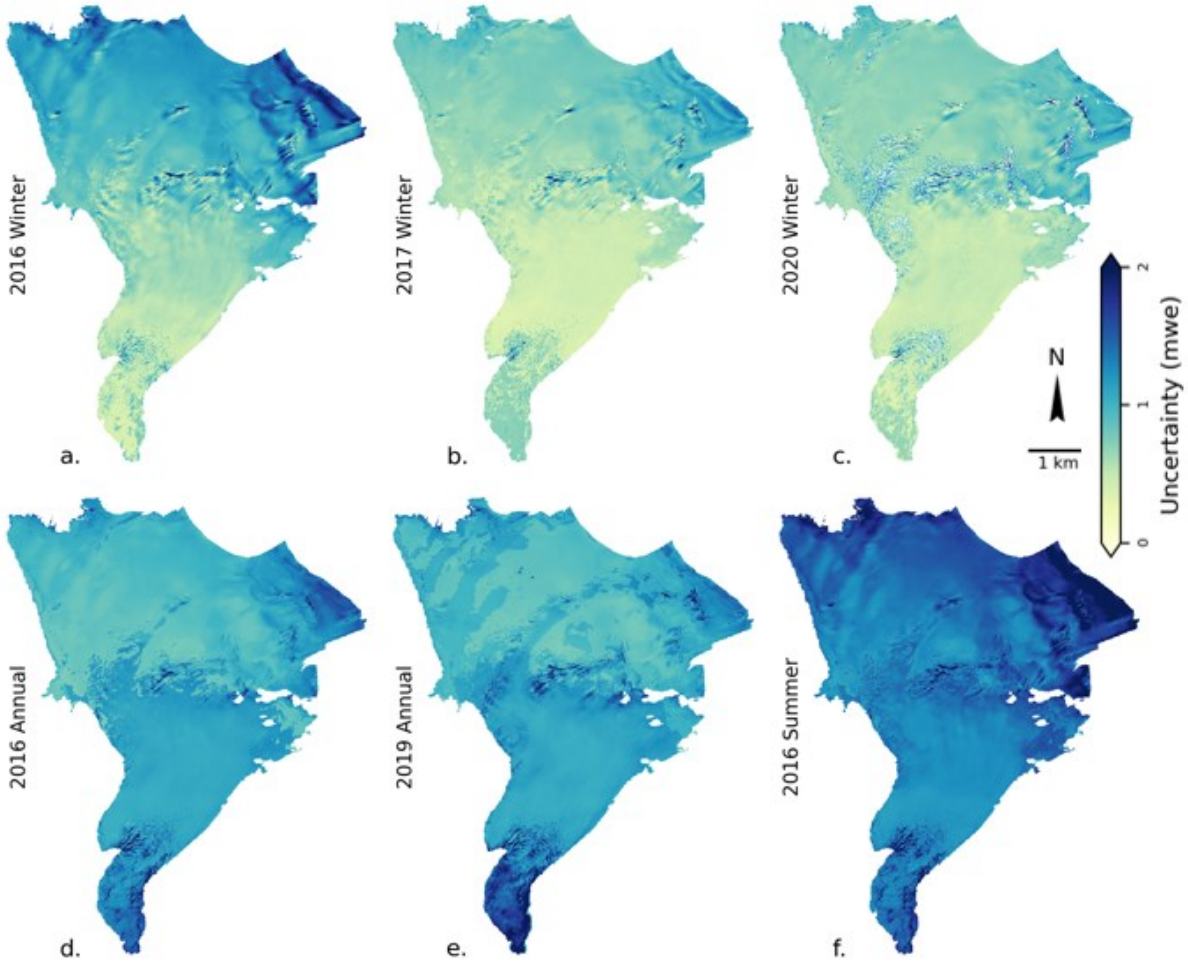

Figure 25: Distributed mass balance uncertainties in each time period, calculated from GPR emergence velocities. Uncertainties in mass balance using modeled emergence velocities are smaller.

7. DISCUSSION

7.1 Emergence Velocity Measurement Methods

The three methods presented for measuring emergence velocity showed generally good agreement with each other. Modelled and GPR emergence velocities were within 1 m/yr across the majority of the glacier area (above 800 m elevation), and within 2 m/yr near the terminus. Median stake-derived emergence velocities varied by up to 2 m/yr, with the largest differences near the terminus and at the highest elevation stakes.

Stake-derived emergence velocities showed significant variability between individual measurements at single stakes (Figure 16). This variability can be attributed to multiple factors: seasonal to annual variations in ice flow, small scale spatial variability in emergence velocity, confounding effects of ice emergence and firn compaction in the accumulation zone, and uncertainties in the measurements (stake tilt, GPS/theodolite precision, difficulties in calculating expected vertical displacement). The variability observed here shows that caution should be used when extrapolating sparse stake emergence velocity measurements across larger spatial and temporal scales, and that using the average of multiple years of data can give more reliable results. These observations may be more easy implemented and added to existing mass balance campaigns than the GPR or modelling approaches to measuring emergence velocities.

The modelled emergence method relies on having knowledge of the average annual mass balance profiles, a task which can be logistically difficult and prone to bias. Surface mass balance modelling approaches, or novel remote sensing techniques, could minimize the amount of in-situ data required and allow emergence velocities to be estimated on a regional scale using this method.

The GPR emergence method presented in this study gives promising results for calculating distributed emergence velocities. Inter-annual similarities (Figure 11) show the ability for limited years of more intensive data collection to be used to derive spatially distributed emergence velocities. This approach, as has been suggested in previous studies (Réveillet et al., 2020) offers the ability to measure emergence velocities over wider and finer spatial scales than point stake measurements allow and is a more direct measurement than modelling approaches. However, ice emergence can only be measured over the winter (when minimal ablation occurs) and as such cannot capture seasonal variations.

When deriving glacier-wide emergence velocities using the GPR or modelling method, a calibration is often necessary to ensure that glacier-wide ice emergence is equal to zero and follows mass continuity. Here, this calibration was accomplished in the modelled emergence velocities by assuming the balance profiles used were systematically biased and were corrected by applying a constant correction factor to emergence velocities across all elevations. For GPR derived emergence velocities, the calibration was done by assuming that the non-zero glacier-wide average emergence velocity was due to misaligned winter DEMs, which was resolved by applying a vertical adjustment to the DEM to bring the net emergence to zero.

7.2 Previous Stake Emergence Velocity Studies

While significant variability in emergence velocities was observed in the majority of mass-balance stakes used in this study, the largest variabilities were at stakes nearest the terminus in both the historical and modern stake datasets. The spatiotemporal variations found here will be compared to previous studies which measured emergence velocities using mass balance stakes.

Significant inter-annual and spatial variability in emergence velocities near the terminus have been observed in studies on two mountain glaciers in western Canada (Beedle et al., 2014) and the French Alps (Vincent et al., 2021) from dense stake networks ($n \approx 20$). A long-term stake array spanning the entire elevation range of Kesselwandferner (Austria) captured similarly large inter-annual variabilities in stake emergence velocities between 1965 and 1985, during which the glacier was advancing and had horizontal ice flow velocities of comparable magnitude to Wolverine Glacier (Stocker-Waldhuber et al., 2019). However, in the period since 1985 the glacier has been retreating, has significantly decreased horizontal flow velocities (~10–20 m/yr), and has exhibited stable emergence velocities. A year-long investigation by Réveillet et al. (2020) in the slow flowing (~10 m/yr) accumulation zone of a glacier in the French Alps found no significant variability in the emergence velocities of five stakes at monthly timescales, yet significant spatial variability.

In the context of this study, the pre-1985 measurements from Stocker-Waldhuber et al. (2019) are most similar in magnitude and variability to the stake emergence record at Wolverine Glacier. The significant spatial variability observed in multiple studies (Beedle et al., 2014; Réveillet et al., 2020; Vincent et al., 2021) suggests that the combination of small-scale spatial variabilities in the emergence velocity field, a dynamically changing glacier geometry and mass balance patterns, and inherent uncertainties in the emergence velocity calculation, could be a cause of the observed variability in this study.

No significant correlation between individual measurements of horizontal and emergence velocities was observed in any stakes, suggesting that short term (seasonal to annual) variations in horizontal velocities cannot be assumed to lead directly to changes in magnitude of emergence

velocities. However, over longer time periods this seems to be the case (i.e., Stocker-Waldhuber et al., 2019).

7.3 Mass Balance Measurements

Geodetic mass-balance measurements showed good agreement with in-situ derived point mass-balance (average RMSE of 0.42 m w.e.), mass-balance profiles (RMSE 1.24 m w.e. across all elevation bands in all annual and seasonal time periods), and glacier-wide mass balances (RMSE of 0.47 m w.e. across all time periods) using both the distributed and profile methods.

Over annual time periods, glacier-wide balances from geodetic measurements outperformed the in-situ measurements which require geodetic calibration to account for systematic bias (O'Neel et al., 2019). These differences can be seen in the in-situ balance profiles (Figure 22) which show a more positive mass balance over all elevation bands. Geodetic and in-situ winter mass balance estimates in 2016 and 2017 show differences similar to those found in a previous study measuring winter mass balance distributions on Wolverine Glacier (McGrath et al., 2018). These comparisons support previous studies suggesting the current stake network does not capture the full spatial variability of mass balance processes on Wolverine Glacier (O'Neel et al., 2019), which is a common problem in the glaciological method (e.g., Zemp et al., 2013; Klug et al., 2018).

The demonstrated ability to measure the spatial distribution of mass balance processes on seasonal and annual scales is novel in glaciological literature. Historically, attempts to understand these processes (accumulation and ablation) have been hampered by the limited distributed in-situ observations that were available, and difficulties with expanding in-situ observations to wider and finer spatial scales. The fully distributed geodetic balances open the

opportunity to understand how accumulation and ablation patterns are influenced by variations in terrain and climate. Improving our understanding of these mass balance processes can inform scientists on how mass balance campaigns can be best designed to capture the variability in mass balance across glacier surfaces.

Many regional glacier models (Radić et al., 2014; Clarke et al., 2015; Rounce et al., 2020) use mass balance profiles as inputs rather than glacier-wide or fully spatially distributed mass balances. The balance profile results presented here show that this geodetic approach can generate invaluable data for calibration and testing of these models.

The vertical co-registration of winter DEMs remains a limitation for geodetic winter balance measurements in areas with complete snow cover. This can be a significant source of error, as shown by the vertical calibration of winter DEMs which were necessary in this study (up to 1.17 m) even after initial alignment attempts.

7.4 Dynamic Terminus Characteristics

An overarching theme in the emergence velocity and mass balance measurements is that the terminus of Wolverine Glacier behaves distinctly from the upper glacier and is undergoing dynamic changes. Seasonal variations in emergence velocity observed in the stake data (Figure 13) were most pronounced at the stake closest to the terminus, with velocities even being negative (submerging) in the mid-summer (with zero emergence being within the range of uncertainty). The greater magnitude of seasonality in emergence velocities is consistent with the more significant seasonality in horizontal velocities for lower elevation regions of the glacier in both the historical and modern stake datasets (Figure 14). However, horizontal velocities and

emergence velocities near the terminus vary inversely, with highest emergence velocities occurring in the mid-winter when the horizontal velocities are at their lowest.

The narrow width of the glacier in this area near its terminus compared to higher elevations is a possible driver of these distinct seasonal variations. Small variations in flow velocities in the wide bench above the terminus (~1000 m elevation, Figure 5) can introduce large ice fluxes into the lower glacier, which must be accommodated for by either increased/decreased horizontal ice flow or dynamic ice thickening/thinning (i.e. emergence or submergence). The precise spatiotemporal pattern of the terminus's response to such a change in incoming flux would determine how this accommodation occurs. The current observations do not provide the spatial or temporal detail needed to fully investigate the dynamics at play but suggest that it is complex.

The declining magnitude of ice emergence as you approach the terminus of Wolverine Glacier, which is captured in both modelled and GPR emergence velocities, and declining horizontal ice velocities as captured in stake GNSS measurements, shows that the glacier is undergoing a dynamic response to mass loss in the 21st century. Ice melt near the terminus is outpacing the rate of ice influx, leaving the remaining ice "disconnected" from the main glacier and leading to more rapid thinning of the terminus than the rest of the glacier.

Similar patterns of glacier retreat and emergence velocities were observed on Kesselwandferner (Stocker-Waldhuber et al., 2019), with the horizontal and emergence velocities of the lowest elevation stake decreasing over time before eventually being lost to ice melt and glacier retreat. Decreasing magnitudes of emergence velocity near the terminus of Findelengletscher were found using the same modelling approach that is employed in this study (Sold et al., 2013).

Modelled emergence velocities on Wolverine Glacier captured this spatial pattern in the 2008–12 and 2015–19 periods, with a sharper inflection seen in the more recent period. The pattern was not seen in earlier periods (1972–79, 1972–95), suggesting it is a recent development. Other glaciers with similar thinning patterns to Wolverine may show a similar pattern of declining emergence velocity at the terminus, and may limit the applicability of previous studies of emergence velocities that were focused on areas near their respective glaciers' termini (i.e., Beedle et al., 2014; Vincent et al., 2021).

The dynamic nature of Wolverine Glacier's lowest elevations makes geodetic mass balance measurements more difficult. Variability in emergence velocities which are difficult to constrain and limited in-situ observations increase the uncertainty in our measurements (Figure 22). More detailed investigation of the spatiotemporal patterns in this area, in the context of the wider glacier dynamics, may be needed to provide reliable geodetic mass balance measurements of the terminus.

7.5 Future Directions

Many new directions of research could be pursued from the analyses presented here. The GPR emergence velocity measurement method should be applied to additional glaciers with ongoing mass-balance campaigns in order to further test its abilities and provide a wider array of ground-truth observations against which modelling efforts can be compared.

If the mass-balance modelled method for deriving emergence velocities can be shown to provide realistic values in varying mass balance regimes, then it would be a relatively simple task to expand seasonal geodetic mass balance methods to a regional scale (e.g., Alaska and NW Canada-wide). Glacier-specific emergence velocity fields could be derived by combining

physically based mass-balance models with published glacier thinning rates (Hugonnet et al., 2021). Automated satellite photogrammetry and ICESat-2 tracks could then be used to measure distributed mass balances over short timeframes (~3 months for ICESat-2 repeat tracks, and dependent on the glacier-specific availability of high-resolution stereo satellite imagery).

Further studies on Wolverine Glacier could investigate emergence velocity variations on a finer spatiotemporal scale than is considered here. This could be approached by a dense stake network (i.e., 50 m separation in a grid pattern) over a small area that are measured on ~monthly scales. Monthly GPR surveys and lidar/SfM flights over a small area could reveal additional small-scale variations. While doing so over the entire glacier surface would not be feasible, having such dense measurements in the context of the wider dynamics at play on Wolverine Glacier would be invaluable. Such studies should be done in areas of the glacier which are relatively stable (i.e. especially not the terminus). Such studies could allow mass balance changes to be measured geodetically on smaller spatial and temporal scales than are investigated here (i.e. 1 m, monthly) which would be invaluable in understanding the physical processes that govern glacier mass balance.

Three-dimensional ice flow models provide a promising approach for deriving emergence velocities but were not investigated here. Precise knowledge of the glacier geometry is needed to implement these models, but ice thickness is unknown and not well constrained for Wolverine Glacier. Modelling approaches to determining ice thickness are promising (Farinotti et al., 2019), but do not necessarily provide the accuracy and precision needed for fine-scale modelling at the glacier scale. Conducting ice thickness surveys at Wolverine Glacier would make it one of the most ideal glaciers in the world on which to conduct precise glacier modelling studies, given the

wide array of mass-balance, meteorological, and associated observations/studies that have been conducted here over the decades.

Lastly, while firn compaction in cold environments such as the Greenland and Antarctic ice sheets have been the subject of many studies, firn compaction on temperate alpine glaciers such as Wolverine is poorly understood. Future work should investigate the process of firn compaction in these environments such that its impact on geodetic mass balances can be better constrained.

8. CONCLUSIONS

Three methods for measuring emergence velocities across the surface of Wolverine Glacier were investigated. These emergence velocities, in conjunction with a firn compaction model, were used in geodetic measurements of surface mass balance over three winters, one summer, and two annual time periods. Multiple spatially and temporally extensive datasets available for Wolverine Glacier were leveraged to allow intercomparison of multiple methodologies and gave the ability to evaluate the performance of each.

Geodetic approaches were able to accurately measure point balance at mass-balance stake locations (RMSE = 0.62 m w.e., n = 41), end-of-winter GPR-derived snow depths (mean RMSE = 0.35 m w.e., n = 9025 10x10 m grid cells), and glacier-wide mass balances (RMSE = 0.47 m w.e.). Over the two annual time periods investigated, geodetic methods outperformed in-situ methods, which require geodetic calibration over decadal time periods to remove systematic biases.

Key differences revealed by the three emergence velocity measurement methods suggest that small scale (seasonal and 10–100 m) spatiotemporal variations in ice dynamics may be significant, particularly in areas undergoing dynamic changes such as the retreating and thinning terminus of Wolverine Glacier. Caution should be used when spatially and temporally extrapolating limited point measurements of emergence velocity.

This analysis offers a comprehensive assessment of multiple approaches for measuring emergence velocities over varying temporal and spatial scales. The distributed geodetic balance products represent a step forward in our ability to understand the physical processes that govern glacier mass balance. The methods are simple enough to implement that they can be easily

applied to other glaciers around the globe. The balance products presented here, and future campaigns to measure distributed geodetic mass balances, will serve as valuable tools for the development and testing of models related to glacier mass balance processes.

As high-resolution geodetic products continue to become more widely available (for example: CryoSat, ICESat-2, satellite stereo-photogrammetry, airborne lidar), the results presented here highlight the potential for these products to be leveraged to measure short term mass balance changes of mountain glaciers by constraining the effects of firn compaction and emergence velocities. Such datasets will advance our understanding of changes in alpine environments, offering the opportunity to prepare for their effects on human-environmental systems.

9. DATA AVAILABILITY

All datasets used in this project are freely available via the US Geological Survey Benchmark Glacier website: https://www2.usgs.gov/landresources/lcs/glacierstudies/benchmark.asp.

Meteorological data may be found at: Baker, E. H., Peitzsch, E. H., Sass, L. C., Miller, Z. S. and Whorton, E. N., 2019, High altitude weather station data at USGS Benchmark Glaciers (ver. 1.0, July 2019): U.S. Geological Survey data release, https://doi.org/10.5066/P9EUXIPE.

Geodetic data may be found at: McNeil, C. J., Florentine, C. E., Bright, V. A. L., Fahey, M. J., McCann, E., Larsen, C. F., Thoms, E. E., Shean, D. E., McKeon, L. A., March, R. S., Keller, W., Whorton, E. N., O'Neel, S.,and Baker, E. H., 2019, Geodetic data for USGS benchmark glaciers: orthophotos, digital elevation models, and glacier boundaries (ver 1.0, September 2019): U.S. Geological Survey data release, https://doi.org/10.5066/P9R8BP3K.

Mass balance input data and glacier-wide solutions may be found at: McNeil, C. J., Sass, L. C., Florentine, C. E., Baker, E. H., Peitzsch, E. H., Whorton, E. N., Miller, Z. S., Fagre, D. B., Clark, A. M. and O'Neel, S. R., 2016, Glacier-wide mass balance and compiled data inputs: USGS benchmark glaciers (ver. 5.0, March 2021): U.S. Geological Survey data release, https://doi.org/10.5066/F7HD7SRF.

Raw GPR data may be found at: O'Neel, S., McGrath, D., Wolken, G. J., Candela, S. G., Sass, L. C., McNeil, C. J., Baker, E. H., Babcock, E. L., Loso, M. G., Arendt, A. A., Whorton, E. N., Burgess, E. W., Gusmeroli, A., 2018, Ground Penetrating Radar Data on North America Glaciers, ver 2.1, September, 2018: U.S. Geological Survey data release, https://doi.org/10.5066/F7M043G7.

10. REFERENCES

Baker EH, Peitzsch EH, Sass L, Miller ZS and Whorton EN (2019) High Altitude Weather Station Data at USGS Benchmark Glaciers. (doi:10.5066/P9EUXIPE)

Beedle MJ, Menounos B and Wheate R (2014) An evaluation of mass-balance methods applied to Castle creek Glacier, British Columbia, Canada. J. Glaciol. 60(220), 262–276 (doi:10.3189/2014jog13j091)

Belart JMC, Berthier E, Magnússon E, Anderson LS, Pálsson F, Thorsteinsson T, Howat IM, Aðalgeirsdóttir G, Jóhannesson T and Jarosch AH (2017) Winter mass balance of Drangajökull ice cap (NW Iceland) derived from satellite sub-meter stereo images. The Cryosphere 11(3), 1501–1517 (doi:10.5194/tc-11-1501-2017)

Cauvy-Fraunié S and Dangles O (2019) A global synthesis of biodiversity responses to glacier retreat. Nat Ecol Evol 3(12), 1675–1685 (doi:10.1038/s41559-019-1042-8)

Cuffey, KM and Paterson, WSB (2010) The Physics of Glaciers, 4th Edn. Oxford: Butterworth-Heinemann

Ciracì E, Velicogna I and Swenson S (2020) Continuity of the Mass Loss of the World's Glaciers and Ice Caps From the GRACE and GRACE Follow-On Missions. Geophys. Res. Lett. 47(9) (doi:10.1029/2019gl086926)

Clarke GKC, Jarosch AH, Anslow FS, Radić V and Menounos B (2015) Projected deglaciation of western Canada in the twenty-first century. Nature Geosci. 8(5), 372–377 (doi:10.1038/ngeo2407)

Cogley J, Hock R, Rasmussen LA, Arendt AA, Bauder A, Braithwaite R J, Jansson P, Kaser G, Möller M, Nicholson L and Zemp M (2011) Glossary of glacier mass balance and related terms. IHP-VII technical documents in hydrology, 86.

Deems JS, Painter TH and Finnegan DC (2013) Lidar measurement of snow depth: a review. J. Glaciol. 59(215), 467–479 (doi:10.3189/2013jog12j154)

Farinotti D, Huss M, Fürst JJ, Landmann J, Machguth H, Maussion F and Pandit A (2019) A consensus estimate for the ice thickness distribution of all glaciers on Earth. Nat. Geosci. 12(3), 168–173 (doi:10.1038/s41561-019-0300-3)

Gardner AS, Moholdt G, Cogley JG, Wouters B, Arendt AA, Wahr J, Berthier E, Hock R, Pfeffer WT, Kaser G, Ligtenberg SRM, Bolch T, Sharp MJ, Hagen JO, van den Broeke MR and Paul F (2013) A Reconciled Estimate of Glacier Contributions to Sea Level Rise: 2003 to 2009. Science 340(6134), 852–857 (doi:10.1126/science.1234532)

Helfricht K, Schöber J, Seiser B, Fischer A, Stötter J and Kuhn M (2012) Snow accumulation of a high alpine catchment derived from LiDAR measurements. Adv. Geosci. 32, 31–39 (doi:10.5194/adgeo-32-31-2012)

Helfricht K, Kuhn M, Keuschnig M and Heilig A (2014) Lidar snow cover studies on glaciers in the Ötztal Alps (Austria): comparison with snow depths calculated from GPR measurements. The Cryosphere 8(1), 41–57 (doi:10.5194/tc-8-41-2014)

Herron MM and Langway CC Jr (1980) Firn Densification: An Empirical Model. J. Glaciol. 25(93), 373–385 (doi:10.3189/s0022143000015239)

Hersbach H, Bell B, Berrisford P, Hirahara S, Horányi A, Muñoz-Sabater J, Nicolas J, Peubey C, Radu R, Schepers D, Simmons A, Soci C, Abdalla S, Abellan X, Balsamo G, Bechtold P, Biavati G, Bidlot J, Bonavita M, Chiara G, Dahlgren P, Dee D, Diamantakis M, Dragani R, Flemming J, Forbes R, Fuentes M, Geer A, Haimberger L, Healy S, Hogan RJ, Hólm E, Janisková M, Keeley S, Laloyaux P, Lopez P, Lupu C, Radnoti G, Rosnay P, Rozum I, Vamborg F, Villaume S and Thépaut J (2020) The ERA5 global reanalysis. Q.J.R. Meteorol. Soc. 146(730), 1999–2049 (doi:10.1002/qj.3803)

Hock R, Bliss A, Marzeion B, Giesen RH, Hirabayashi Y, Huss M, Radic V and Slangen ABA (2019) GlacierMIP – A model intercomparison of global-scale glacier mass-balance models and projections. J. Glaciol. 65(251), 453–467 (doi:10.1017/jog.2019.22)

Hugonnet R, McNabb R, Berthier E, Menounos B, Nuth C, Girod L, Farinotti D, Huss M, Dussaillant I, Brun F and Kääb A (2021) Accelerated global glacier mass loss in the early twenty-first century. Nature 592(7856), 726–731 (doi:10.1038/s41586-021-03436-z)

Huss M (2013) Density assumptions for converting geodetic glacier volume change to mass change. The Cryosphere 7(3), 877–887 (doi:10.5194/tc-7-877-2013)

Huss M and Hock R (2015) A new model for global glacier change and sea-level rise. Front. Earth Sci. 3 (doi:10.3389/feart.2015.00054)

Huss M, Bookhagen B, Huggel C, Jacobsen D, Bradley RS, Clague JJ, Vuille M, Buytaert W, Cayan DR, Greenwood G, Mark BG, Milner AM, Weingartner R and Winder M (2017)

Toward mountains without permanent snow and ice. Earth's Future 5(5), 418–435 (doi:10.1002/2016ef000514)

Huss M and Hock R (2018) Global-scale hydrological response to future glacier mass loss. Nature Clim Change 8(2), 135–140 (doi:10.1038/s41558-017-0049-x)

Immerzeel WW, Lutz AF, Andrade M, Bahl A, Biemans H, Bolch T, Hyde S, Brumby S, Davies BJ, Elmore AC, Emmer A, Feng M, Fernández A, Haritashya U, Kargel JS, Koppes M, Kraaijenbrink PDA, Kulkarni AV, Mayewski PA, Nepal S, Pacheco P, Painter TH, Pellicciotti F, Rajaram H, Rupper S, Sinisalo A, Shrestha AB, Viviroli D, Wada Y, Xiao C, Yao T and Baillie JEM (2019) Importance and vulnerability of the world's water towers. Nature 577(7790), 364–369 (doi:10.1038/s41586-019-1822-y)

Klug C, Bollmann E, Galos SP, Nicholson L, Prinz R, Rieg L, Sailer R, Stötter J and Kaser G (2018) Geodetic reanalysis of annual glaciological mass balances (2001–2011) of Hintereisferner, Austria. The Cryosphere 12(3), 833–849 (doi:10.5194/tc-12-833-2018)

Kohler J, Moore J, Kennett M, Engeset R and Elvehøy H (1997) Using ground-penetrating radar to image previous years' summer surfaces for mass-balance measurements. Ann. Glaciol. 24, 355–360 (doi:10.3189/s0260305500012441)

Kovacs A, Gow AJ and Morey RM (1995) The in-situ dielectric constant of polar firn revisited. Cold Regions Science and Technology 23(3), 245–256 (doi:10.1016/0165-232x(94)00016-q)

Kulp SA and Strauss BH (2019) New elevation data triple estimates of global vulnerability to sea-level rise and coastal flooding. Nat Commun. 10(1) (doi:10.1038/s41467-019-12808-z)

Lane SN, Bakker M, Gabbud C, Micheletti N and Saugy J-N (2017) Sediment export, transient landscape response and catchment-scale connectivity following rapid climate warming and Alpine glacier recession. Geomorphology 277, 210–227 (doi:10.1016/j.geomorph.2016.02.015)

Larsen CF, Burgess E, Arendt AA, O'Neel S, Johnson AJ and Kienholz C (2015) Surface melt dominates Alaska glacier mass balance. Geophys. Res. Lett. 42(14), 5902–5908 (doi:10.1002/2015gl064349)

Machguth H, Eisen O, Paul F and Hoelzle M (2006) Strong spatial variability of snow accumulation observed with helicopter-borne GPR on two adjacent Alpine glaciers. Geophys. Res. Lett. 33(13) (doi:10.1029/2006gl026576)

Marshak S and Repcheck J (2009) Essentials of geology. New York: WW Norton.

Marzeion B, Jarosch AH and Hofer M (2012) Past and future sea-level change from the surface mass balance of glaciers. The Cryosphere 6(6), 1295–1322 (doi:10.5194/tc-6-1295-2012)

Mayo, LR, March, RS and Trabant, DC (1992) Air temperature and precipitation data, 1967-88 Wolverine Glacier Basin, Alaska. USGS Open File Report 1991–246.

Mayo, LR, Trabant, DC and March, RS (2004) A 30-Year record of surface mass balance (1966–95), and motion and surface altitude (1975–95) at Wolverine Glacier, Alaska. USGS Open File Report 2004–1069.

McGrath D, Sass L, O'Neel S, Arendt A, Wolken G, Gusmeroli A, Kienholz C and McNeil C (2015) End-of-winter snow depth variability on glaciers in Alaska. J. Geophys. Res. Earth Surf. 120(8), 1530–1550 (doi:10.1002/2015jf003539)

McGrath D, Sass L, O'Neel S, McNeil C, Candela SG, Baker EH and Marshall H-P (2018) Interannual snow accumulation variability on glaciers derived from repeat, spatially extensive ground-penetrating radar surveys. The Cryosphere 12(11), 3617–3633 (doi:10.5194/tc-12-3617-2018)

Mcneil CJ, Florentine CE, Bright VAL, Fahey MJ, McCann E, Larsen CF, Thoms EE, Shean DE, McKeon LA, March RS, Keller W, Whorton EN, O'Neel SR and Baker EH (2019) Geodetic Data for USGS Benchmark Glaciers: Orthophotos, Digital Elevation Models, and Glacier Boundaries. (doi:10.5066/P9R8BP3K)

Milner AM, Khamis K, Battin TJ, Brittain JE, Barrand NE, Füreder L, Cauvy-Fraunié S, Gíslason GM, Jacobsen D, Hannah DM, Hodson AJ, Hood E, Lencioni V, Ólafsson JS, Robinson CT, Tranter M and Brown LE (2017) Glacier shrinkage driving global changes in downstream systems. Proc Natl Acad Sci USA 114(37), 9770–9778 (doi:10.1073/pnas.1619807114)

Moore RD, Fleming SW, Menounos B, Wheate R, Fountain A, Stahl K, Holm K and Jakob M (2009) Glacier change in western North America: influences on hydrology, geomorphic hazards and water quality. Hydrol. Process. 23(1), 42–61 (doi:10.1002/hyp.7162)

Nolan M, Larsen C and Sturm M (2015) Mapping snow depth from manned aircraft on landscape scales at centimeter resolution using structure-from-motion photogrammetry. The Cryosphere 9(4), 1445–1463 (doi:10.5194/tc-9-1445-2015)

Nuth C and Kääb A (2011) Co-registration and bias corrections of satellite elevation data sets for quantifying glacier thickness change. The Cryosphere 5(1), 271–290 (doi:10.5194/tc-5-271-2011)

O'Neel S, McNeil C, Sass LC, Florentine C, Baker EH, Peitzsch E, McGrath D, Fountain AG and Fagre D (2019) Reanalysis of the US Geological Survey Benchmark Glaciers: long-term insight into climate forcing of glacier mass balance. J. Glaciol. 65(253), 850–866 (doi:10.1017/jog.2019.66)

Pelto BM, Menounos B and Marshall SJ (2019) Multi-year evaluation of airborne geodetic surveys to estimate seasonal mass balance, Columbia and Rocky Mountains, Canada. The Cryosphere 13(6), 1709–1727 (doi:10.5194/tc-13-1709-2019)

Pope A, Willis IC, Palsson F, Arnold NS, Rees WG, Bjornsson H and Grey L (2016) Elevation change, mass balance, dynamics and surging of Langjökull, Iceland from 1997 to 2007. J. Glaciol. 62(233), 497–511 (doi:10.1017/jog.2016.55)

Pritchard HD (2019) Asia's shrinking glaciers protect large populations from drought stress. Nature 569(7758), 649–654 (doi:10.1038/s41586-019-1240-1)

Radić V, Bliss A, Beedlow AC, Hock R, Miles E and Cogley JG (2013) Regional and global projections of twenty-first century glacier mass changes in response to climate scenarios from global climate models. Clim Dyn 42(1–2), 37–58 (doi:10.1007/s00382-013-1719-7)

Reeh N (2008) A nonsteady-state firn-densification model for the percolation zone of a glacier. J. Geophys. Res. 113(F3) (doi:10.1029/2007jf000746)

Réveillet M, Vincent C, Six D, Rabatel A, Sanchez O, Piard L and Laarman O (2020) Spatio-temporal variability of surface mass balance in the accumulation zone of the Mer de Glace, French Alps, from multitemporal terrestrial LiDAR measurements. J. Glaciol. 67(261), 137–146 (doi:10.1017/jog.2020.92)

RGI Consortium (2017) Randolph Glacier Inventory – A Dataset of Global Glacier Outlines: Version 6.0: Technical Report, Global Land Ice Measurements from Space, Colorado, USA. Digital Media. (doi: https://doi.org/10.7265/N5-RGI-60)

Roe GH, Christian JE and Marzeion B (2021) On the attribution of industrial-era glacier mass loss to anthropogenic climate change. The Cryosphere 15(4), 1889–1905 (doi:10.5194/tc-15-1889-2021)

Rounce DR, Hock R and Shean DE (2020) Glacier Mass Change in High Mountain Asia Through 2100 Using the Open-Source Python Glacier Evolution Model (PyGEM). Front. Earth Sci. 7 (doi:10.3389/feart.2019.00331)

Sass LC, Loso MG, Geck J, Thoms EE and McGrath D (2017) Geometry, mass balance and thinning at Eklutna Glacier, Alaska: an altitude-mass-balance feedback with implications for water resources. J. Glaciol. 63(238), 343–354 (doi:10.1017/jog.2016.146)

Shean DE, Bhushan S, Montesano P, Rounce DR, Arendt A and Osmanoglu B (2020) A Systematic, Regional Assessment of High Mountain Asia Glacier Mass Balance. Front. Earth Sci. 7 (doi:10.3389/feart.2019.00363)

Sold L, Huss M, Hoelzle M, Andereggen H, Joerg PC and Zemp M (2013) Methodological approaches to infer end-of-winter snow distribution on alpine glaciers. J. Glaciol. 59(218), 1047–1059 (doi:10.3189/2013jog13j015)

Sold L, Huss M, Eichler A, Schwikowski M and Hoelzle M (2015) Unlocking annual firn layer water equivalents from ground-penetrating radar data on an Alpine glacier. The Cryosphere 9(3), 1075–1087 (doi:10.5194/tc-9-1075-2015)

Spensberger, Clemens. “Ice Can Flow like Ketchup.” Scisnack, 4 Oct. 2013, www.scisnack.com/2013/10/04/ice-can-flow-like-ketchup/.

Stocker-Waldhuber M, Fischer A, Helfricht K and Kuhn M (2019) Long-term records of glacier surface velocities in the Ötztal Alps (Austria). Earth Syst. Sci. Data 11(2), 705–715 (doi:10.5194/essd-11-705-2019)

Stoffel M and Huggel C (2012) Effects of climate change on mass movements in mountain environments. Progress in Physical Geography: Earth and Environment 36(3), 421–439 (doi:10.1177/0309133312441010)

van Beusekom, AE, O'Neel, S, March, RS, Sass, LC and Cox, LH (2010) Re-analysis of Alaskan benchmark glacier mass-balance data using the index method. U.S. Geological Survey Scientific Investigations Report 2010(5247), 16.

Vincent C, Cusicanqui D, Jourdain B, Laarman O, Six D, Gilbert A, Walpersdorf A, Rabatel A, Piard L, Gimbert F, Gagliardini O, Peyaud V, Arnaud L, Thibert E, Brun F and Nanni U (2021) Geodetic point surface mass balances: a new approach to determine point surface mass balances on glaciers from remote sensing measurements. The Cryosphere 15(3), 1259–1276 (doi:10.5194/tc-15-1259-2021)

WCRP Global Sea Level Bedget Group (2018) Global sea-level budget 1993–present. Earth Syst. Sci. Data 10(3), 1551–1590 (doi:10.5194/essd-10-1551-2018)

Winstral A, Elder K and Davis RE (2002) Spatial Snow Modeling of Wind-Redistributed Snow Using Terrain-Based Parameters. J. Hydrometeor 3(5), 524–538 (doi:10.1175/1525-7541(2002)003<0524:ssmowr>2.0.co;2)

Welling JT, Árnason Þ and Ólafsdottír R (2015) Glacier tourism: a scoping review. Tourism Geographies 17(5), 635–662 (doi:10.1080/14616688.2015.1084529)

World Glacier Monitoring Service (WGMS) (2020) Fluctuations of Glaciers Database. (doi:10.5904/WGMS-FOG-2020-08)

Wouters B, Gardner AS and Moholdt G (2019) Global Glacier Mass Loss During the GRACE Satellite Mission (2002-2016). Front. Earth Sci. 7 (doi:10.3389/feart.2019.00096)

Zemp M, Huss M, Thibert E, Eckert N, McNabb R, Huber J, Barandun M, Machguth H, Nussbaumer SU, Gärtner-Roer I, Thomson L, Paul F, Maussion F, Kutuzov S and Cogley JG (2019) Global glacier mass changes and their contributions to sea-level rise from 1961 to 2016. Nature 568(7752), 382–386 (doi:10.1038/s41586-019-1071-0)